



## Complementary *operando* insights into the activation of multicomponent selective propylene oxidation catalysts



Matthias Stehle<sup>a</sup>, Abhijeet Gaur<sup>a,b</sup>, Sebastian Weber<sup>a,b</sup>, Thomas L. Sheppard<sup>a,b</sup>, Michael Thomann<sup>c</sup>, Achim Fischer<sup>c</sup>, J.-D. Grunwaldt<sup>a,b,\*</sup>

<sup>a</sup>Institute for Chemical Technology and Polymer Chemistry, Karlsruhe Institute of Technology, Engesserstr. 20, 76131 Karlsruhe, Germany

<sup>b</sup>Institute of Catalysis Research and Technology, Karlsruhe Institute of Technology, Hermann-von-Helmholtz-Platz 1, 76344 Eggenstein-Leopoldshafen, Germany

<sup>c</sup>Evonik Operations GmbH, Rodenbacher Chaussee 4, 63457 Hanau-Wolfgang, Germany

### ARTICLE INFO

#### Article history:

Received 30 January 2021

Revised 11 August 2021

Accepted 16 August 2021

Available online 27 October 2021

Special Issue of Journal of Catalysis dedicated to Professor Jerzy Haber and Professor Robert K. Grasselli

#### Keywords:

Selective oxidation

Propylene

Acrolein

Mixed metal oxides

Bismuth molybdates

X-ray absorption spectroscopy

X-ray diffraction

Raman spectroscopy

*Operando*

Synchrotron radiation

### ABSTRACT

Two Bi–Mo–Co–Fe–O catalysts were synthesized by flame spray pyrolysis and tested for their catalytic performance in selective oxidation of propylene to acrolein. Pronounced structural changes during temperature-programmed oxidation and reaction were observed by *operando* X-ray absorption spectroscopy, X-ray diffraction, Raman spectroscopy, and thermogravimetric analysis. During oxidative treatment, mainly binary oxide phases ( $\alpha$ -Bi<sub>2</sub>Mo<sub>3</sub>O<sub>12</sub>,  $\beta$ -CoMoO<sub>4</sub>, Fe<sub>2</sub>(MoO<sub>4</sub>)<sub>3</sub>) were observed, but single (MoO<sub>3</sub>) or ternary (Bi<sub>3</sub>(FeO<sub>4</sub>)(MoO<sub>4</sub>)<sub>2</sub>) oxides also formed depending on the relative elemental catalyst composition. During propylene oxidation, the reduction of Fe<sup>3+</sup> to Fe<sup>2+</sup> led to a strong rise in activity and induced further phase transformations. MoO<sub>3</sub> was found to be unselective towards acrolein but was essential in binding other single oxides. The formation of  $\beta$ -Co<sub>0.7</sub>Fe<sub>0.3</sub>MoO<sub>4</sub> and Bi<sub>3</sub>(FeO<sub>4</sub>)(MoO<sub>4</sub>)<sub>2</sub> as well as their synergistic interplay with  $\alpha$ -Bi<sub>2</sub>Mo<sub>3</sub>O<sub>12</sub> are key factors for high performance. The combination of complementary *operando* methods was crucial to reveal new structure–activity/selectivity correlations, therefore bridging the knowledge gap between simplified model systems and complex applied catalysts.

© 2021 The Authors. Published by Elsevier Inc. This is an open access article under the CC BY license (<http://creativecommons.org/licenses/by/4.0/>).

### 1. Introduction

Selective oxidation reactions, which have been a major focus in the work of Jerzy Haber and Robert K. Grasselli, are key steps in chemical industry for the functionalization of hydrocarbons [1–3]. Among these, the selective oxidation of propylene to acrolein plays an important role. Global acrolein production sums up to  $\sim 5 \cdot 10^6$  t a<sup>-1</sup> [4], and optimization of this process has therefore attracted increased research attention within the last years [5]. Bismuth molybdates (Bi–Mo–O) are well-known as highly selective catalysts in the oxidation of propylene to acrolein [6]. The addition of metals such as Fe, Ni, and Co has furthermore led to dramatic increases in performance *via* the presence of synergistically acting

mixtures of individual phases [7–9]. In turn, the structural complexity of the original bismuth molybdate systems has continuously increased, making it difficult to obtain a full understanding of the workings of the catalyst, particularly the link between structure, activity and selectivity. Many studies have focused on basic or binary systems of bismuth molybdates ( $\alpha$ -Bi<sub>2</sub>Mo<sub>3</sub>O<sub>12</sub>,  $\beta$ -Bi<sub>2</sub>Mo<sub>2</sub>O<sub>9</sub>,  $\gamma$ -Bi<sub>2</sub>MoO<sub>6</sub>), leading to different and occasionally conflicting statements about their activity and selectivity towards acrolein [10–16]. Even though the redox properties and thus the activity and selectivity depend on the Bi–Mo–O structure [17–19], these properties change when bismuth molybdates are intermixed leading to improved performance [19].

Despite their superior performance, relatively few studies have addressed the complex nature of multicomponent catalysts, allowing only a basic understanding of their working principles. Since the catalyst structure is affected by the composition as well as the preparation method [8], deconvoluting complex phase mixtures into all individual phases and their interactions is difficult

\* Corresponding author at: Institute for Chemical Technology and Polymer Chemistry, Karlsruhe Institute of Technology, Engesserstr. 20, 76131 Karlsruhe, Germany (J.-D. Grunwaldt).

E-mail address: [grunwaldt@kit.edu](mailto:grunwaldt@kit.edu) (J.-D. Grunwaldt).

to achieve. Nevertheless, in the 1970s different particle models were developed in an attempt to categorize the key functions of multicomponent systems. First, Wolfs and co-workers [20,21] proposed a simplified particle model for the quaternary system  $\text{Bi}_1\text{Fe}_3\text{-Co}_8\text{Mo}_{12}\text{O}_x$ . It consisted of a core formed mainly by  $\text{CoMoO}_4$  (host structure) and islands of  $\text{Fe}_2(\text{MoO}_4)_3/\text{FeMoO}_4$  ( $\text{Fe}^{3+/2+}$  redox couple improving oxygen transport). The shell was made up by bismuth molybdates, acting as active centers. Subsequently, the model was revised mainly by including  $\text{MoO}_3$  [8]. Over time, general trends for such multicomponent catalysts were established as reviewed by Moro-Oka and Ueda [8]. To increase the performance of Bi–Mo–O based systems, the simultaneous addition of a divalent  $\text{M}_I^{2+}$  and a trivalent  $\text{M}_{II}^{3+}$  metal cation, each with an ionic radius  $<0.8 \text{ \AA}$ , is required, summing up to the overall elemental composition Bi–Mo– $\text{M}_I^{2+}$ – $\text{M}_{II}^{3+}$ –O (e.g., with  $\text{M}_I^{2+} = \text{Fe, Co, Ni}$ ; and  $\text{M}_{II}^{3+} = \text{Fe, Cr, Al}$ ). For the Bi–Mo–Co–Fe–O system, multiple phases including  $\alpha\text{-Bi}_2\text{Mo}_3\text{O}_{12}$ ,  $\gamma\text{-Bi}_2\text{MoO}_6$ ,  $\alpha\text{-}/\beta\text{-CoMoO}_4$ ,  $\text{Co}_x\text{Fe}_{1-x}\text{MoO}_4$ ,  $\text{Bi}_3(\text{FeO}_4)(\text{MoO}_4)_2$ ,  $\beta\text{-FeMoO}_4$ ,  $\text{Fe}_2(\text{MoO}_4)_3$ , and free  $\text{MoO}_3$  have been reported [20–29], highlighting the complex nature. Hence, the mutual influence of the different phases on the catalytic performance of the finally active catalyst is still not fully clear yet.

Since it is generally accepted for Bi–Mo–O and Bi–Mo–Co–Fe–O catalysts that propylene oxidation to acrolein proceeds via the Mars–van Krevelen mechanism [8,22,30–34], lattice oxygen plays a crucial role within the catalytic cycle. In four-component Bi–Mo–Co–Fe–O, iron molybdates (i.e.,  $\text{Fe}_2(\text{MoO}_4)_3$ ,  $\text{FeMoO}_4$ ) or mixed cobalt iron molybdates ( $\text{Co}_x\text{Fe}_{1-x}\text{MoO}_4$ ) are ascribed for oxygen activation and migration through the bulk to the active center (Bi–Mo–O) [20,22,23,35]. Thus, oxygen activation and its insertion into propylene probably take place at different sites [7,8,34]. Consequently, a close contact of the different phases is essential to enable their cooperation for increased catalytic performance [7,13,36]. To study the phase cooperation in Bi–Mo–Co–Fe–O catalysts, and to correlate their structure with activity, mainly (mechanical) mixtures of individual phases were used [24–26,35,37]. Even though such mixtures enabled a basic understanding of the catalyst working principles, their simplified nature does not fully represent real multicomponent catalysts. On the other hand, studies on multicomponent catalysts [20,23] often fail to fully unveil the numerous structural changes occurring on stream [28,29]. Thus, complementary methods are required to follow the changes induced by calcination, which is typically carried out after synthesis [20,23,27,28,38–40], and under reaction conditions (e.g., reduction, phase formation/transformation/decomposition, morphological changes) [21,23,25,26,28,41,42] and to finally correlate these changes to catalytic function. Ideally, this demands a combination of *in situ* [23,35] and *operando* [27] studies in order to draw meaningful conclusions.

In the present work, we studied the structural evolution of two exemplary Bi–Mo–Co–Fe–O catalysts [20,28] during temperature-programmed treatment under oxidizing (TPO) and reaction conditions (TPRM) by complementary *operando* methods. The aim was to better understand phase formation and evolution during potential thermal pretreatment (i.e., calcination) and during activation of the catalysts as well as the influence of specific phases on catalytic performance. Due to the complex nature of the investigated systems, complementary techniques were necessary to ensure a profound understanding of the structural changes observed with respect to elemental composition, gas atmosphere, and temperature. Thermal analysis, synchrotron X-ray absorption spectroscopy (XAS), synchrotron X-ray diffraction (XRD) combined with Rietveld refinement, and Raman spectroscopy (RS) were applied to identify crystalline and amorphous phases, the evolution and transformation of active phases, short and long range structure as well as the oxidation states of the elements present. Hence, we aimed at detailed *operando* insights into the processes during

catalyst activation to revise our understanding of Bi–Mo–Co–Fe–O catalysts and the metal oxide phases present therein.

## 2. Materials and methods

### 2.1. Catalyst preparation

Two Bi–Mo–Co–Fe–O catalysts, which differ in their relative elemental composition (FSP–1 and FSP–2, see Table 1), were synthesized via flame spray pyrolysis (FSP) in a single step using a setup similar to that reported by Madler et al. [43] and our earlier studies [19,28]. In general, FSP is an attractive method for the synthesis of multicomponent Bi–Mo–Co–Fe–O catalysts as it leads to a homogenous elemental distribution, small crystallite size, and large specific surface area [28]. The total volume of the precursor solution was 250 mL with a total metal precursor concentration of 0.30 M (see Table 1). First, bis(2,4-pentanedionato)molybdenum(VI) dioxide ( $\text{MoO}_2(\text{acac})_2$ , Alfa Aesar) was dissolved in 60 mL methanol (MeOH, VWR Chemicals) and sonicated until a clear solution was obtained. Bismuth(III) acetate ( $\text{Bi}(\text{OAc})_3$ , Sigma Aldrich) and 40 mL acetic acid (HOAc, Sigma Aldrich) were added to the solution and sonicated again until no more solids were visible. Subsequently, cobalt(II) nitrate hexahydrate ( $\text{Co}(\text{NO}_3)_2 \cdot 6\text{H}_2\text{O}$ , Merck) and tris(2,4-pentanedionato)iron(III) ( $\text{Fe}(\text{acac})_3$ , Fluka Chemika) were added. A total volume of 250 mL was achieved by adding a 3/2 mixture (v/v) of MeOH/HOAc. The solution was sonicated for additional 30 min.

For spraying, the obtained solution was transferred into a 50 mL syringe (Henke–Sass Wolf). A syringe pump (Legato 210, KD Scientific) was used to achieve a constant solution dosage rate of  $5 \text{ mL min}^{-1}$  through the FSP nozzle. The nozzle itself consisted of a holder system and an insertable steel needle (GA22/60 mm/PST3, Hamilton). The dosed liquid was finely dispersed at the needle tip by  $5.0 \text{ L min}^{-1} \text{ O}_2$  (N48, Air Liquide) at 3 bar back-pressure. The needle-surrounding flame ring, which ignites the solution, was formed by a mixture of  $0.75 \text{ L min}^{-1} \text{ CH}_4$  (N25, Air Liquide) and  $1.6 \text{ L min}^{-1} \text{ O}_2$ . Controlled gas dosage was realized by mass flow controllers (Bronkhorst). The brownish powder obtained was collected on a glass fiber filter ( $\varnothing = 24 \text{ cm}$ , GF6, GE Healthcare) via a vacuum pump (R5, Busch GmbH). The filter and needle holder system were constantly water cooled. For each 50 mL syringe batch a new filter was used. Last, the obtained batches were scratched off the filters, combined, and sieved through a  $600 \mu\text{m}$  mesh. The resulting powders were used as-prepared unless stated elsewhere.

### 2.2. Catalytic tests and conventional catalyst characterization

Catalytic performance tests in selective propylene oxidation were performed using a fixed-bed testing setup with an on-line gas chromatograph (GC) for product analysis. The testing procedure comprised different temperature points ( $T = 345\text{--}400 \text{ }^\circ\text{C}$ ) at which the total gas flow was varied ( $\text{N}_2/\text{O}_2/\text{C}_3\text{H}_6/\text{H}_2\text{O} = 70/14/8/8 \text{ vol\%}$ ,  $\text{WHSV}_{\text{C}_3\text{H}_6} = 1.14\text{--}3.42 \text{ h}^{-1}$ ). The catalysts were characterized *ex situ* before and after catalytic testing by inductively coupled plasma optical emission spectrometry (ICP–OES), nitrogen physisorption, Raman spectroscopy (RS), laboratory powder X-ray diffraction (XRD), X-ray absorption spectroscopy (XAS), and transmission electron microscopy with energy-dispersive X-ray spectroscopy (TEM–EDX). Details about testing and *ex situ* characterization are given in the Supporting Information.

### 2.3. In situ and operando catalyst characterization

#### 2.3.1. In situ TG–DSC–MS and TG–MS under reaction conditions

Simultaneous thermogravimetry, differential scanning calorimetry and mass spectrometry (TG–DSC–MS) was performed

**Table 1**  
Target metal ratios and precursor amounts used for FSP.

Sample	Metal ratio / mol%				Precursor mass / g			
	Bi	Mo	Co	Fe	Bi(OAc) <sub>3</sub>	MoO <sub>2</sub> (acac) <sub>2</sub>	Co(NO <sub>3</sub> ) <sub>2</sub> ·6H <sub>2</sub> O	Fe(acac) <sub>3</sub>
FSP-1	7.2	59.2	24.8	8.8	2.08	14.49	5.42	2.33
FSP-2	4.2	50.0	33.3	12.5	1.22	12.23	7.27	3.32

with a STA 449 F3 Jupiter<sup>®</sup> and a QMS 403 Aëolos (NETZSCH) using alumina crucibles for TG–DSC–MS, and quartz glass crucibles in the case of TG–MS studies. Due to catalytic activity of the thermocouples present at the TG–DSC–MS holder, only TG–MS experiments (without DSC) could be performed under propylene containing atmosphere. 25.1 mg of the as-prepared powders after FSP were filled in the glass crucible for TG–MS and ~10 mg were filled in the alumina crucible for TG–DSC–MS. An empty second crucible was used as reference during TG–DSC–MS studies. The whole setup was flushed at ambient temperature with the corresponding gas mixture (oxidizing atmosphere: Ar/O<sub>2</sub> = 80/20 vol%; reaction gas mixture: Ar/O<sub>2</sub>/C<sub>3</sub>H<sub>6</sub> = 80/12/8 vol%; 100 mL min<sup>-1</sup> total flow) overnight. The dosage of H<sub>2</sub>O in the gas feed for the reaction gas mixture was not possible due to instrumental limitations. The measurement sequence was as follows: isothermal at 30 °C for 2 h, heating to 600 °C (5 °C min<sup>-1</sup>), 10 min isothermal, fast cooling to ambient temperature. A reference measurement performed with an empty crucible was subtracted from the obtained TG data of the samples to account for the buoyancy effect. Mass changes correspond to the first mass datapoint of the isothermal period at 30 °C.

### 2.3.2. Operando setup for spectroscopy and diffraction studies

Further *in situ* and *operando* studies were performed by XAS, XRD, and RS using a fixed-bed quartz glass capillary microreactor [44] (sieve fraction 100–200 μm, Ø = 1 mm, 10 μm wall thickness, Hilgenberg GmbH). The same gas mixtures (oxidizing conditions (TPO): He/O<sub>2</sub> = 88/12 vol%; reaction conditions (TPRM): He/O<sub>2</sub>/C<sub>3</sub>H<sub>6</sub>/H<sub>2</sub>O = 72/12/8/8 vol%; 10 mL min<sup>-1</sup> total flow) and temperature ranges (100–600 °C) were applied in all cases. Prior to the TPO/TPRM experiments, the temperature inside the capillary was calibrated and the individual heating efficiency was considered. Hence, temperatures given for *in situ* and *operando* experiments refer to the calibrated value inside the capillary, which was measured by an inserted type K thermocouple, and in the case of XRD by the thermal lattice expansion of a silver reference. Controlled gas dosing was achieved by mass flow controllers (Bronkhorst) with water vapor dosed using a self-built heated steel saturator. Fast switching between different gas atmospheres was realized by a 4-way valve (VICI). Gas lines were heated to 180 °C to prevent water and product condensation. An on-line mass spectrometer (OMNI Star GSD 320, Pfeiffer Vacuum) was used to analyze the product gas mixture.

### 2.3.3. Operando X-ray absorption spectroscopy

*Operando* XAS was performed sequentially at all four metal edges (Mo K, Bi L<sub>3</sub>, Co K, Fe K) in a single run in transmission mode at the ROCK beamline (SOLEIL, Saint-Aubin, France). The storage ring was operated at 2.75 GeV under top-up mode at 500 mA. The unique infrastructure available at ROCK enables fast edge changing [45,46], and thus the acquisition of all four metal edges during a single run. The Si(220) monochromator was used for data acquisition at Mo K-edge, while the Si(111) monochromator was used for acquisition at the Bi L<sub>3</sub>-, Co K-, and Fe K-edges, respectively (see Table S4). The as-prepared samples after FSP synthesis were mixed with α-Al<sub>2</sub>O<sub>3</sub> (1/3 (m/m) catalyst/α-Al<sub>2</sub>O<sub>3</sub>), ground, pressed, granulated, and sieved to give the desired fraction. About 7 mg of the sieve fraction was placed in a quartz glass capillary,

resulting in a bed length of 10 mm. The capillary was heated with a gas blower (FMB Oxford) in the range of 100–600 °C (1.5 °C min<sup>-1</sup>). XAS data was acquired in the middle of the catalyst bed at 2 Hz. To acquire data for all metals in a single experiment, a loop in the sequence of Mo K-, Bi L<sub>3</sub>- and Fe K-/Co K-edge (recorded in a single scan) was performed. At constant temperatures, acquisition at Mo K-edge lasted 5 min, whereas at Bi L<sub>3</sub>- and Fe K-/Co K-edges it lasted 10 min each. For better temperature resolution, the acquisition time during heating was reduced to 2 min (Mo K), 4 min (Bi L<sub>3</sub>) and 4 min (Fe K/Co K), respectively. One complete acquisition loop during heating lasted ~12 min. Spectra of the initial and final state of the catalysts during the *operando* measurements were recorded under He atmosphere. The spectra of one acquisition period were averaged to produce a single spectrum for each edge. Energy calibration, averaging, background subtraction, and normalization were done by the beamline software [72]. For further data treatment, the software package IFEFFIT [47] was used. More details of XAS data acquisition and analysis are given in the [Supporting Information](#).

### 2.3.4. Operando synchrotron X-ray diffraction

The *operando* XRD studies were conducted at the Swiss-Norwegian beamline (SNBL) BM01 at the European Synchrotron Radiation Facility (ESRF, Grenoble, France). The experiments were performed with a monochromatic beam (λ = 0.62779 Å, ~250x250 μm<sup>2</sup>). The detector (PILATUS 2 M, Dectris) was calibrated using LaB<sub>6</sub> powder. 2D diffraction patterns were recorded in the middle of the catalyst bed using the PILATUS@SNBL diffractometer [48] with an acquisition time of 30 s. Azimuthal integration of the acquired 2D images was done with Bubble software [48]. About 5 mg of the undiluted sample was filled in the capillary, resulting in a bed length of 5 mm. For heating of the capillary reactor (100–600 °C, 5 °C min<sup>-1</sup>), a gas blower available at the beamline was used. Sequential Rietveld refinement (2θ range = 3–25°) was performed with the software TOPAS [49] (v6, Bruker AXS) using references available in the Inorganic Crystal Structure Database (ICSD, see Table S6). From Rietveld refinement crystalline phase amounts, crystallite sizes and lattice parameters were obtained. More information about sequential Rietveld refinement can be found in the [Supporting Information](#).

### 2.3.5. Operando Raman spectroscopy

*Operando* Raman spectroscopy was performed with an inVia Raman spectrometer (Renishaw) equipped with a frequency doubled Nd:YAG laser (532 nm, ~100 mW at the source). The laser beam was focused on the capillary via a video and optical fiber probe (Renishaw) with a long working distance objective. For heating of the capillary reactor (100–600 °C, 1.5 °C min<sup>-1</sup>), a gas blower (LE MINI SENSOR KIT, Leister Technologies) was used. Raman spectra were recorded continuously (10% laser intensity, 120 s acquisition time, 2400 lines mm<sup>-1</sup> grating resulting in a spectral range of ~50–1300 cm<sup>-1</sup>). The laser intensity at the sample was measured prior to the experiments and amounted to ~4.3 mW. To account for localized probing of the heterogeneous multicomponent systems (Ø<sub>laser spot</sub> = ~70 μm), the fiber optic was moved periodically (1 period min<sup>-1</sup>) parallel to the capillary (center ± 1 mm) via an automated xy-stage. This produced averaged spectra repre-

senting the whole sample rather than individual heterogeneous regions. Data treatment, which included cosmic ray removal, noise filtering, truncation, and baseline subtraction, was performed with WiRE 4.4 (Renishaw). Assignment of Raman bands was carried out based on the metal oxide phases listed in Table S5 and the references listed therein.

### 3. Results and discussion

#### 3.1. Catalytic performance and conventional characterization of FSP-made Bi–Mo–Co–Fe–O catalysts

Two Bi–Mo–Co–Fe–O catalysts with different metal ratios (see Table 1) were prepared by FSP. ICP–OES results (see Table S1) indicated a good match ( $\sim 0.2\%$ ) between the calculated and experimentally determined metal composition. This underlines the precise control over elemental composition for FSP-made multi-component catalysts. Furthermore, the metal fractions did not change during testing, indicating high stability within the time scale investigated, *i.e.*, no Mo loss due to the formation of volatile Mo compounds in the presence of water [5,50,51].  $N_2$  physisorption revealed a surface area of 82 and  $80 \text{ m}^2 \text{ g}^{-1}$  for FSP-1 and FSP-2 in the as-prepared state (denoted as –F), respectively. For comparison, classical preparation methods like co-precipitation typically lead to small surface areas of maximum  $7 \text{ m}^2 \text{ g}^{-1}$  [8]. Additionally, the laboratory XRD patterns of the as-prepared samples (Fig. 1c) exhibited only a few, rather broad reflections, indicating small crystallite sizes and a high amount of amorphous phases. The few reflections present could be assigned to  $\beta$ -CoMoO<sub>4</sub>/ $\beta$ -Co<sub>0.7</sub>Fe<sub>0.3</sub>MoO<sub>4</sub> and CoO. Amorphous phases were detected by RS, including corresponding bands for  $\beta$ -CoMoO<sub>4</sub>/ $\beta$ -Co<sub>0.7</sub>Fe<sub>0.3</sub>MoO<sub>4</sub> (Fig. 1d). Furthermore, TEM–EDX (Table S2 and Table S3) indicated a rather good mixing of the elements.

Subsequently, both as-prepared samples were tested for their catalytic performance in selective oxidation of propylene in a

lab-scale fixed-bed reactor (for details see Supporting Information). The testing results for FSP-1 and FSP-2 are given in Fig. 1a and b, respectively. Beside the target product acrolein, the by-products CO, CO<sub>2</sub> (both are cumulated to CO<sub>x</sub>), and acrylic acid were observed. In general, both catalysts exhibited high propylene conversion compared to bismuth molybdates [19] combined with high selectivity towards acrolein. Furthermore, with increasing WHSV the propylene conversion decreased while the acrolein selectivity increased. This trend is similar to binary bismuth molybdates, but the four-component systems showed a far higher activity (propylene conversion increased by a factor of 2–3 for same WHSV values compared to two-component bismuth molybdates [19]). At 345 °C, FSP-1 and FSP-2 were already close to their maximal performance, indicating high activity already in the low temperature range. Notably, FSP-2 showed superior propylene conversion compared to FSP-1, combined with higher acrolein selectivity over the whole temperature range when similar propylene conversion levels are compared. For instance, at 400 °C oven temperature and a similar propylene conversion of  $\sim 60\%$  (different WHSVs), FSP-1 exhibited an acrolein selectivity of 83% and an acrylic acid selectivity of 12%, while FSP-2 was highly selective towards acrolein (90% and 5%, respectively). However, it took more than one day until the first activity point (345 °C,  $1.14 \text{ h}^{-1}$ ) could be acquired due to changes in selectivity as monitored by an on-line oxygen sensor. Differences in activity for the first measurement points at 345 °C might arise from latent changes in catalyst structure/phase composition [5,28,52,53] influencing the performance.

Post-testing characterization revealed a drastic decrease in surface area to 4 (FSP-1–R) and  $3 \text{ m}^2 \text{ g}^{-1}$  (FSP-2–R), respectively. Nevertheless, the catalysts still showed high activity, emphasizing the predominant role of the metal oxide phase composition forming on stream. Additionally, catalytic testing led to increased crystallinity as indicated by sharper XRD reflections and Raman bands (see Fig. 1c and d, respectively). Furthermore, the phase composition

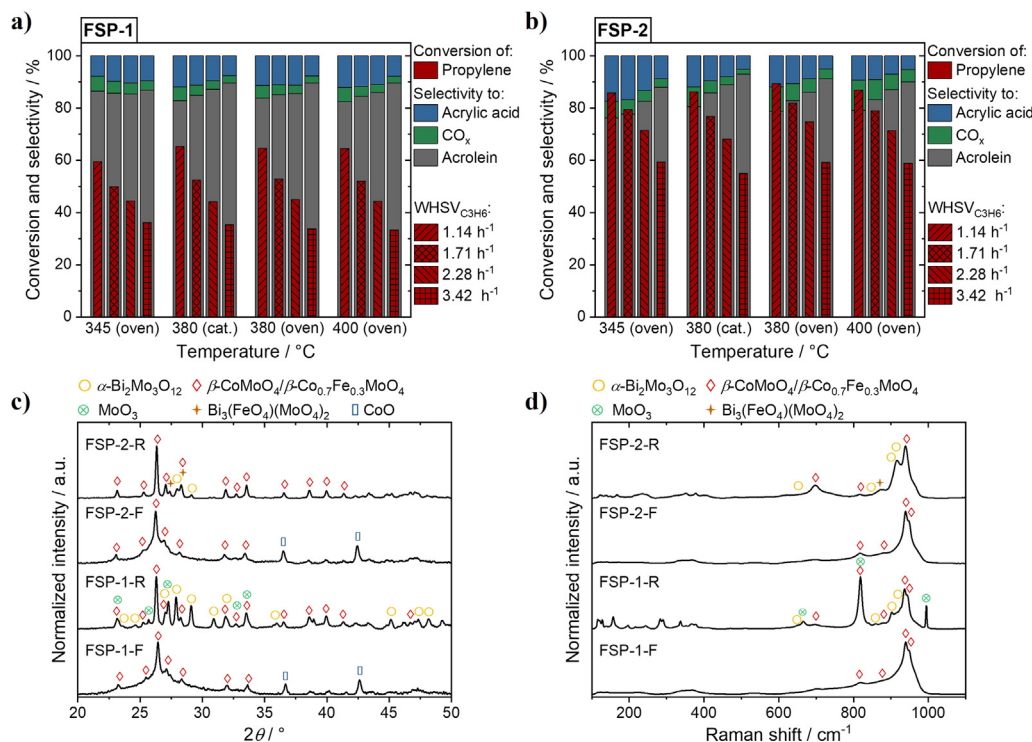


**Fig. 1.** Catalytic testing results and characterization of FSP-made samples. Propylene conversion and product selectivities for FSP-1 (a) and FSP-2 (b) during lab-scale tests in selective oxidation of propylene at different temperatures and WHSVs using a fixed-bed reactor ( $N_2/O_2/C_3H_6/H_2O = 70/14/8/8 \text{ vol}\%$ , 800 mg catalyst). Characterization of FSP-1 and FSP-2 before (–F) and after catalytic testing (–R) with the assignment of phases by XRD (c) and RS (d).

changed as the reflections corresponding to CoO disappeared, while for FSP–1 signals corresponding to MoO<sub>3</sub> and  $\alpha$ -Bi<sub>2</sub>Mo<sub>3</sub>O<sub>12</sub> and for FSP–2 signals assigned to  $\alpha$ -Bi<sub>2</sub>Mo<sub>3</sub>O<sub>12</sub> and Bi<sub>3</sub>FeMo<sub>2</sub>O<sub>12</sub> appeared. The formation and segregation of metal oxide phases as well as an increased particle size were confirmed by TEM–EDX (see Table S2 and Table S3). In the case of FSP–1, regions with an atomic ratio corresponding to Co<sub>0.7</sub>Fe<sub>0.3</sub>MoO<sub>4</sub>, CoMoO<sub>4</sub>,  $\alpha$ -Bi<sub>2</sub>Mo<sub>3</sub>O<sub>12</sub>, and MoO<sub>3</sub> could be revealed after catalytic testing. Notably, the elemental composition at different spots differed drastically, indicating a separation of phases on the nm level. In the case of FSP–2, the variations at the different spots after testing were far less notable compared to FSP–1. Especially the Co/Mo and Fe/Mo ratios were quite constant, indicating the preferential formation of co-located CoMoO<sub>4</sub> and FeMoO<sub>4</sub>, or mixed Co<sub>x</sub>Fe<sub>1-x</sub>MoO<sub>4</sub>. Mo segregation was not observed, pointing towards the absence of MoO<sub>3</sub> in FSP–2. *Ex situ* XAS revealed the reduction of Fe<sup>3+</sup> to Fe<sup>2+</sup>. However, due to phase changes caused by grinding (see Supporting Information) to prepare pellets of the catalysts after testing, *ex situ* XAS data are not further discussed as this data was not considered representative of the catalyst state after testing. Note that phase changes induced by grinding were only found to affect the catalysts after testing.

Overall, *ex situ* characterization highlighted the nano-crystalline nature of both FSP–made catalysts after synthesis. During testing, both catalysts, particularly FSP–2, showed a high activity in propylene oxidation with a high selectivity towards acrolein. However, pronounced crystallization processes and phase transformations took place during time on stream. To evaluate the influence of gas composition and temperature on the formation of phases, *operando* characterization was performed under oxidizing and reaction conditions, in particular to investigate the role of Fe<sup>2+</sup>/Fe<sup>3+</sup> redox couples, which are known to play an important role in the catalytic cycle [8,34].

### 3.2. Phase formation during TPO

First, the structural evolution of the samples under oxidative treatment was investigated as catalysts are often calcined prior to testing. However, little is known about the influence of such a thermal pretreatment on the metal oxide phase composition of Bi–Mo–Co–Fe–O catalysts. Furthermore, the TPO experiments then also serve as a reference for the changes occurring under reaction gas atmosphere. In this way, it is possible to judge the stability of certain metal oxide phases with respect to gas atmosphere, and thus their relevance for catalysis.

#### 3.2.1. *In situ* thermal analysis combined with mass spectrometry

The combined TG–DSC–MS experiments enabled simultaneous monitoring of weight changes (TG), exothermic/endothermic processes (DSC), and gas phase composition (MS) during heating under oxidizing conditions. As shown in Fig. 2, both catalysts exhibited similar TG curves characterized by a weight loss of ~2% from 100 to 350 °C. This weight loss was assigned *via* MS to the desorption/release of H<sub>2</sub>O and the desorption/formation of CO<sub>2</sub>. Subsequently, the mass was almost constant. However, significant differences in the DSC curves and their derivatives were observed for temperatures above 300 °C (see Fig. 2c). While FSP–1 exhibited in the derivative peaks at around 340, 380, 415, 570 (with a broad shoulder towards lower temperatures) and >590 °C, FSP–2 showed peaks at around 345, 365, 445 and 565 °C. This indicates that different phases were formed during the oxidative treatment. Hence, the initial catalyst composition as well as the temperature influence the phase composition of both samples. To investigate the phase formation processes during TPO, complementary experiments were performed by *in situ* XAS, XRD, and RS.

#### 3.2.2. *In situ* X-ray absorption spectroscopy

*In situ* multi-edge XAS was performed to reveal the changes in individual metal constituents during TPO. The induced changes for all four metal edges in the case of FSP–1 are given in Fig. 3a–d.

Mo K-edge X-ray absorption near edge structure (XANES) data exhibits two significant features A and B. Feature A (~20,007 eV) is attributed to the dipole-forbidden/quadrupole-allowed 1s–4d transition, which is primarily associated to tetrahedral geometry like in Fe<sub>2</sub>(MoO<sub>4</sub>)<sub>3</sub>, but also present with weak intensity in distorted octahedral geometry. Feature B (~20,027 eV) is assigned to the dipole-allowed 1s–5p transition and is characteristic for (distorted) octahedral geometry such as in MoO<sub>3</sub> [54]. Comparing the Mo K-edge spectra at 100 °C before and after TPO up to 600 °C revealed an increased tetrahedral nature of Mo coordination (Fig. 3a).

The obtained Mo K-edge XANES spectra during heating (Fig. 3e) were analyzed by linear combination fitting (LCF) using reference compounds for octahedral (*i.e.*, MoO<sub>3</sub>) and tetrahedral (*i.e.*, Fe<sub>2</sub>(MoO<sub>4</sub>)<sub>3</sub>) Mo coordination to follow the temperature-dependent changes during TPO (see Fig. 3f). LCF initially revealed a mixture of both tetrahedral and octahedral nature. During TPO, first a slight decrease in octahedral nature from 41 to 34% up to 330 °C was observed, followed by a short but significant increase up to 38%. This increase indicates the formation of an octahedrally coordinated Mo phase such as MoO<sub>3</sub>. After a plateau until ~450 °C, another phase formation or transition took place as the tetrahedral amount increased from 65 to finally 86% (*e.g.*, formation of Fe<sub>2</sub>(MoO<sub>4</sub>)<sub>3</sub>). The transformation towards more tetrahedral nature was additionally indicated by Fourier transform extended X-ray absorption fine structure (FT EXAFS) fitting (see Table S11) as the coordination number (CN) of Mo–O increased from initially 2.9 to finally 3.5, which is close to the ideal value of 4. Furthermore, an increased ordering/crystallization of the sample took place since the backscattering from higher shells (Mo–Fe and Mo–Mo) significantly increased (see Table S11 and Figure S12).

For the Bi L<sub>3</sub>-edge (Fig. 3b) and Co K-edge (Fig. 3c), the changes in XANES region during TPO were less pronounced, but still provide important information for phase analysis. The white line of Bi L<sub>3</sub>-edge XANES data shifted towards lower energy and mostly matched the spectrum of  $\alpha$ -Bi<sub>2</sub>Mo<sub>3</sub>O<sub>12</sub> in the final state. Feature C, which is characteristic for Bi<sub>3</sub>(FeO<sub>4</sub>)(MoO<sub>4</sub>)<sub>2</sub> (see Figure S10), was absent in this case. For Co K-edge XANES, a weak feature D was present in all spectra revealing octahedral coordination. Additionally, the absence of feature E, which is characteristic for  $\alpha$ -CoMoO<sub>4</sub>, indicates that the sample consisted mostly of  $\beta$ -CoMoO<sub>4</sub> (*c.f.* ref. [55]). Furthermore, FT EXAFS fitting revealed dramatic changes for Co as a pronounced backscattering from higher shells (Co–Co and Co–Mo) was only observed after heat-up, while the Co–Co path at 3.00 Å, present in CoO model, disappeared (see Table S11, Figure S11, and Figure S12). This indicates a transformation of initially present CoO into  $\beta$ -CoMoO<sub>4</sub>.

For the initial state at Fe K-edge (Fig. 3d), features F (~7,114 eV), G (~7,122 eV), and H (~7,132 eV) are similar to those of the Fe<sub>2</sub>(MoO<sub>4</sub>)<sub>3</sub> reference. LCF using Fe<sub>2</sub>(MoO<sub>4</sub>)<sub>3</sub> and Fe<sub>2</sub>O<sub>3</sub> as references revealed a mixture of 53% and 47%, respectively. During TPO, the features F, G, and H were enhanced showing an increased content of Fe<sub>2</sub>(MoO<sub>4</sub>)<sub>3</sub> (66%) and lower Fe<sub>2</sub>O<sub>3</sub> (34%), in line with the results from Mo K-edge. In the FT EXAFS after TPO the Fe–Fe backscattering shifted towards higher distances and the appearance of new Fe–Mo backscattering (see Table S11 and Figure S12) was observed, thus indicating the formation of Fe<sub>2</sub>(MoO<sub>4</sub>)<sub>3</sub> phase during TPO.

In the case of FSP–2, almost the same changes were induced by TPO (see Fig. 4, Figure S13, Figure S14 and Table S12) compared to FSP–1. Mo K-edge XANES data (Fig. 4a, e) showed transition of Mo towards tetrahedral coordination. LCF of Mo K-edge XANES data

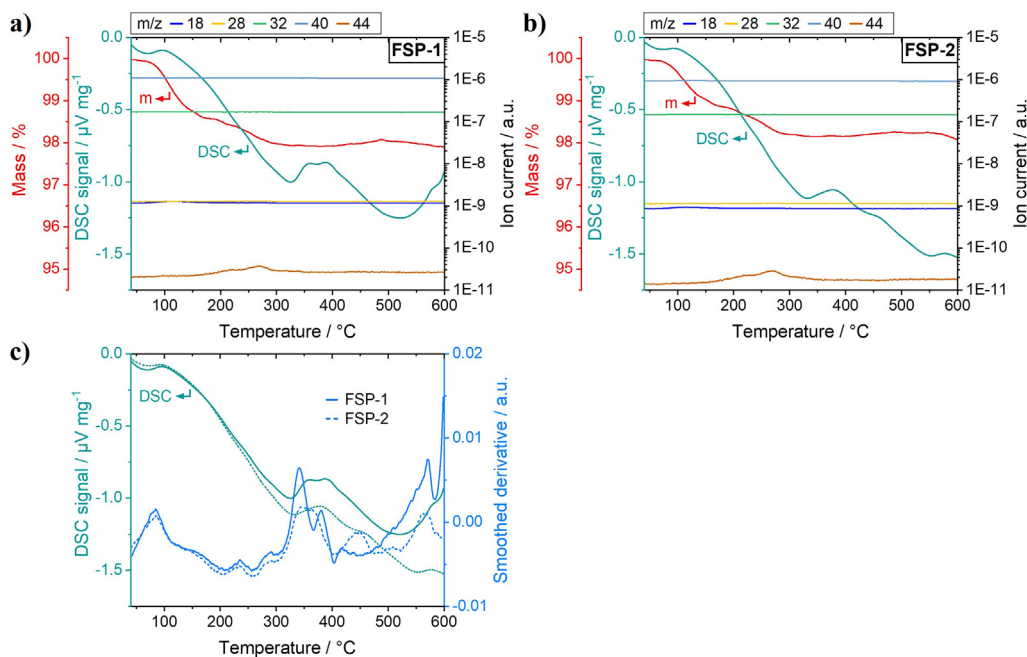


**Fig. 2.** Combined TG–DSC–MS data for FSP–1 (a) and FSP–2 (b) during heating in oxidizing conditions ( $\sim 10$  mg catalyst, Ar/O<sub>2</sub> = 88/12 vol%; 100 mL min<sup>-1</sup> total flow), and comparison of both DSC curves together with the corresponding smoothed derivatives (c). Most intense MS signal for different species with  $m/z$ : 18: H<sub>2</sub>O, 28: CO, 32: O<sub>2</sub>, 40: Ar, 44: CO<sub>2</sub>.

during heating (Fig. 4f) revealed an initial state of 35% MoO<sub>3</sub> (octahedral coordination) and 65% Fe<sub>2</sub>(MoO<sub>4</sub>)<sub>3</sub> (tetrahedral coordination), which is close to the initial state of FSP–1 (41% and 59%, respectively). During heating, the tetrahedral nature increased with a pronounced change from  $\sim 70$  to 82% in the temperature range 330–400 °C. While FSP–1 showed an increase in octahedral nature in this temperature range (Fig. 3f), such a trend was not observed for FSP–2. In comparison, FSP–2 reached tetrahedral nature already at much lower temperatures. Hence, although the final phase composition was similar for both samples, the evolution of the phases involving Mo in sample FSP–2 differed from those in FSP–1.

For Bi L<sub>3</sub>-edge XANES spectra of FSP–2 (Fig. 4b), a shift of the white line towards lower energy was observed as in the case of FSP–1. However, the final spectrum exhibits a feature C ( $\sim 13,460$  eV) similar to that present in the Bi<sub>3</sub>(FeO<sub>4</sub>)(MoO<sub>4</sub>)<sub>2</sub> reference (see Figure S10) but not observed in  $\alpha$ -Bi<sub>2</sub>Mo<sub>3</sub>O<sub>12</sub>. The course of the Bi L<sub>3</sub>-edge XANES spectra during heating (see Figure S13) revealed that the formation of this ternary phase started at  $\sim 400$  °C. The formation of Bi<sub>3</sub>(FeO<sub>4</sub>)(MoO<sub>4</sub>)<sub>2</sub> was further supported by Fe K-edge XANES spectra (Fig. 4d), where LCF using Fe<sub>2</sub>(MoO<sub>4</sub>)<sub>3</sub>, Fe<sub>2</sub>O<sub>3</sub>, and Bi<sub>3</sub>(FeO<sub>4</sub>)(MoO<sub>4</sub>)<sub>2</sub> references revealed contribution of these phases to be 43, 42, and 16% at 600 °C, respectively. For comparison, the phase contribution for initial state at 100 °C was observed to be 47, 47 and 6%, while in the final state after cooling to 100 °C it was 55, 36 and 9%. Here also, Co K-edge XANES data (Fig. 4c) confirmed the presence of  $\beta$ -CoMoO<sub>4</sub>, and FT EXAFS points towards the transformation of CoO into  $\beta$ -CoMoO<sub>4</sub>, similar to FSP–1. FT EXAFS fitting for all edges (see Table S12 and Figure S14) revealed an increased backscattering from higher shells, which is linked both to the formation of new phases and increased structural ordering (*i.e.*, crystallization) during TPO.

In summary, multi-edge XAS revealed pronounced changes for both samples during the course of TPO. While similar results were obtained for Co (mainly present as  $\beta$ -CoMoO<sub>4</sub>), the other constituents Fe, Mo and Bi were (partly) incorporated in different phases. For FSP–1, a unique interim increase in octahedral Mo

coordination indicates the (transient) formation of MoO<sub>3</sub>. Whereas FSP–1 contained mainly binary  $\alpha$ -Bi<sub>2</sub>Mo<sub>3</sub>O<sub>12</sub> and Fe<sub>2</sub>(MoO<sub>4</sub>)<sub>3</sub>, the formation of the ternary phase Bi<sub>3</sub>(FeO<sub>4</sub>)(MoO<sub>4</sub>)<sub>2</sub> was only observed for FSP–2. This reveals that while both samples showed increased long-range order, indicating an increase in particle size most likely due to crystallization, the precise phase formation processes between them differed significantly. As it is challenging to identify all phases present using XAS alone due to the averaging nature of the method, additional techniques sensitive to crystalline and amorphous phases were applied to further study the processes occurring during TPO.

### 3.2.3. In situ synchrotron X-ray diffraction and Raman spectroscopy

Synchrotron XRD combined with Rietveld refinement enabled precise crystalline phase analysis compared to laboratory XRD (see Figure S5), and furthermore allowed quantification of the crystalline phase amounts present. Moreover, RS provided additional complementary insights on amorphous phases. The phase analysis results for both samples during TPO are shown in Fig. 5. Note that an overview of metal oxide phases considered during phase analysis is given in Table S5.

Both as-prepared catalysts showed only the presence of crystalline  $\beta$ -CoMoO<sub>4</sub> and CoO by XRD, while the corresponding Raman spectra exhibited strong features originating from  $\beta$ -CoMoO<sub>4</sub> [56–58]. During heating of FSP–1, reflections corresponding to  $\alpha$ -Bi<sub>2</sub>Mo<sub>3</sub>O<sub>12</sub>, MoO<sub>3</sub> and Fe<sub>2</sub>(MoO<sub>4</sub>)<sub>3</sub> appeared (Fig. 5a, Figure S21). This was in line with the changes observed by RS (Fig. 5c, Figure S21), where characteristic bands of the corresponding phases ( $\alpha$ -Bi<sub>2</sub>Mo<sub>3</sub>O<sub>12</sub> [19,59,60], MoO<sub>3</sub> [28,61], and Fe<sub>2</sub>(MoO<sub>4</sub>)<sub>3</sub> [56,62]) were observed. Due to the formation of new crystalline phases, the amount of  $\beta$ -CoMoO<sub>4</sub> decreased during TPO from initially 95 to finally 39 wt%, which is mainly due to the low crystallinity (nano- and non-crystalline nature) in the initial state. Additionally, the amount of CoO continuously decreased from initially 5 to  $\sim 2$  wt% at 440 °C (subsequently no refinement was possible) indicating that CoO reacted to form other (most likely binary) metal oxide phases.

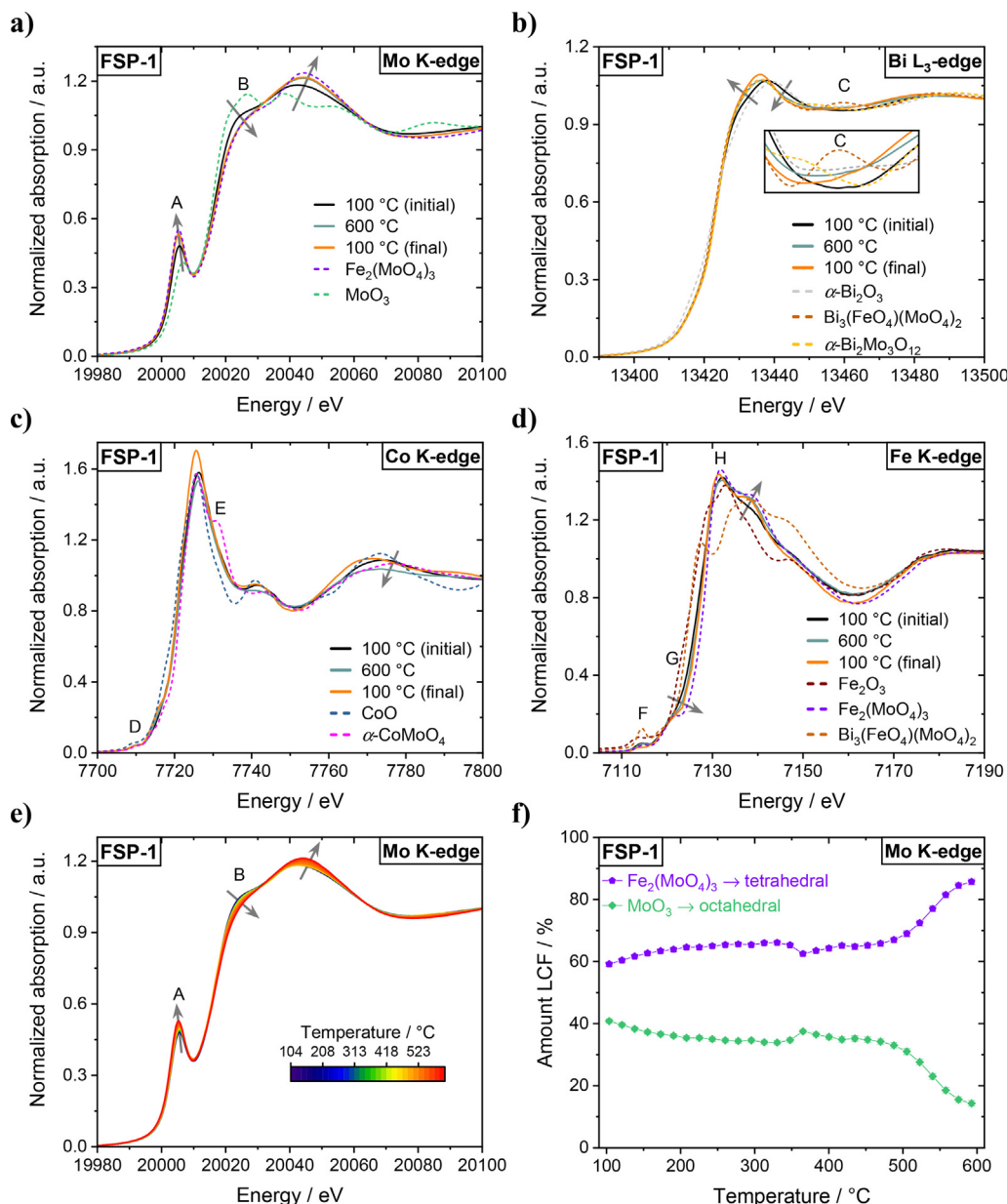


**Fig. 3.** Multi-edge XAS data for FSP-1 during TPO. Normalized XANES spectra for the sample under isothermal conditions and selected reference compounds (dotted lines, recorded at room temperature): Mo K-edge (a), Bi L<sub>3</sub>-edge with zoom on feature C (b), Co K-edge (c), and Fe K-edge (d). Course of Mo K-edge XANES spectra during heating (e), and corresponding LCF results using references for tetrahedral (Fe<sub>2</sub>(MoO<sub>4</sub>)<sub>3</sub>) and octahedral (MoO<sub>3</sub>) Mo coordination geometries (f). Arrows in the figures with XANES spectra point to the direction of observed changes during TPO.

During TPO, MoO<sub>3</sub> was formed starting at ~340 °C (RS), followed by a distinct crystallization (390–440 °C) as revealed by XRD. The MoO<sub>3</sub> phase amount reached a plateau of ~22 wt% in the temperature range of 440–540 °C before it declined to finally 12 wt%. This decline matches well the increase in Fe<sub>2</sub>(MoO<sub>4</sub>)<sub>3</sub>, which has been confirmed by XAS and RS. Thus, this shows the reaction of amorphous Fe<sub>2</sub>O<sub>3</sub> (revealed by XAS) with MoO<sub>3</sub> to Fe<sub>2</sub>(MoO<sub>4</sub>)<sub>3</sub> [63,64] (see Eq. (1)).



Since the amount of MoO<sub>3</sub> and Fe<sub>2</sub>(MoO<sub>4</sub>)<sub>3</sub> were almost constant during isothermal treatment at 600 °C, it can be concluded that all Fe was bound within the Fe<sub>2</sub>(MoO<sub>4</sub>)<sub>3</sub> phase. Furthermore, the formation of crystalline α-Bi<sub>2</sub>Mo<sub>3</sub>O<sub>12</sub> started at 420 °C, while the new Raman band appearing at ~895 cm<sup>-1</sup> could be clearly assigned to α-Bi<sub>2</sub>Mo<sub>3</sub>O<sub>12</sub>. At ~530 °C α-Bi<sub>2</sub>Mo<sub>3</sub>O<sub>12</sub> reached a stable

amount of ~23 wt%, confirming the phase assignment from Bi L<sub>3</sub>-edge XAS. During the isothermal period at 600 °C, no changes in crystalline phase composition could be observed. However, pronounced crystallization processes took place as the crystallite size of all phases increased (see Fig. 5a).

During TPO of FSP-2 (Fig. 5b, d), the same trends for Co containing phases were observed compared to FSP-1. However, the formation of phases was distinctly different from FSP-1, in agreement with XAS. For instance, no crystalline MoO<sub>3</sub> could be observed during TPO for FSP-2. Nevertheless, a very small MoO<sub>3</sub> amount was detected by RS as visible by the characteristic band at 995 cm<sup>-1</sup> in the temperature range of around 350–460 °C (see Figure S23). As for FSP-1, α-Bi<sub>2</sub>Mo<sub>3</sub>O<sub>12</sub> was formed but its crystallization started at higher temperatures of 460 °C, reaching a maximum amount of 17 wt% at ~550 °C. Subsequently, the amount of α-Bi<sub>2</sub>Mo<sub>3</sub>O<sub>12</sub> decreased to 2 wt%, while Bi<sub>3</sub>(FeO<sub>4</sub>)(MoO<sub>4</sub>)<sub>2</sub> was simulta-

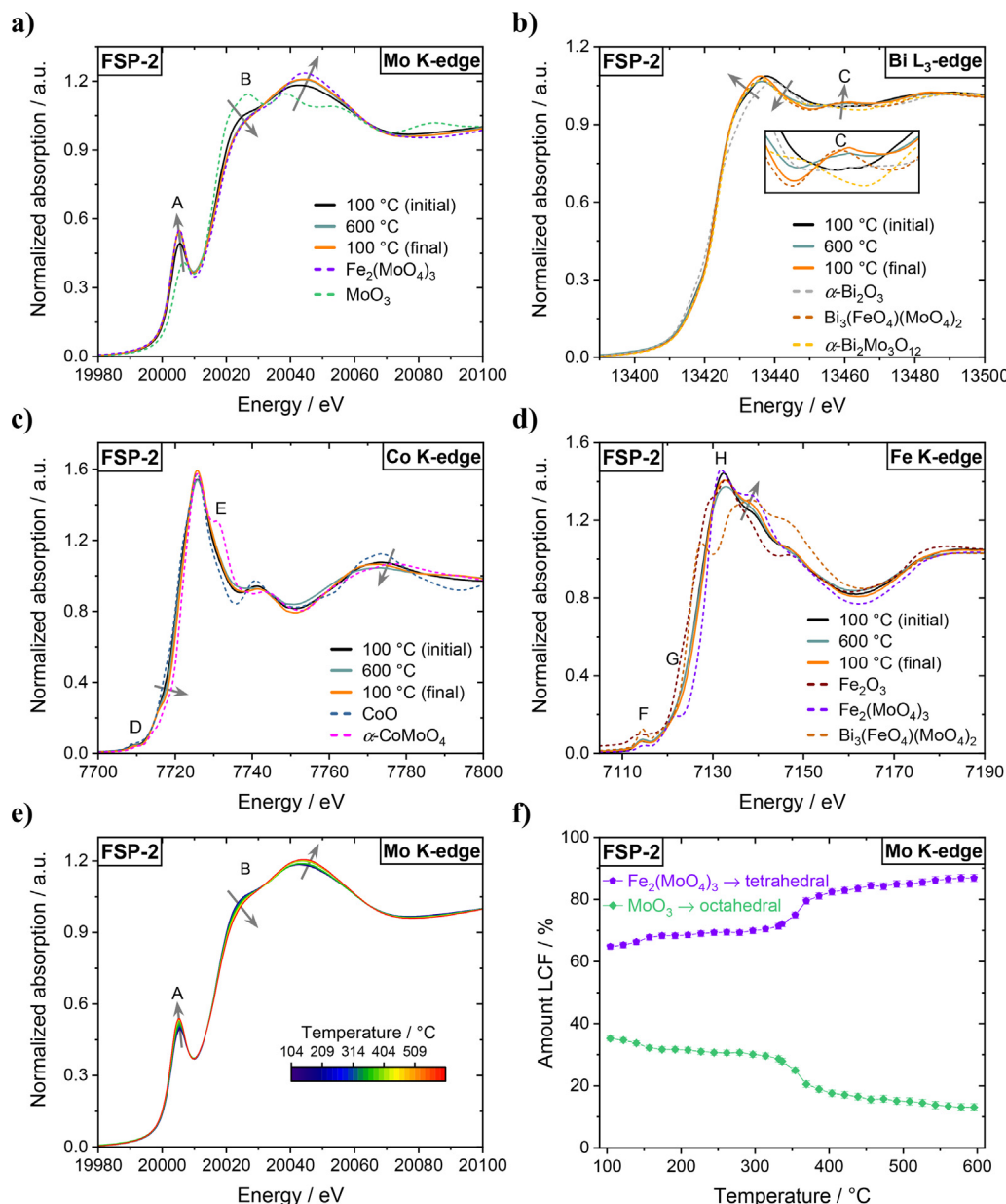


**Fig. 4.** Multi-edge XAS data for FSP-2 during TPO. Normalized XANES spectra for the sample under isothermal conditions and selected reference compounds (dotted lines, recorded at room temperature): Mo K-edge (a), Bi L<sub>3</sub>-edge with zoom on feature C (b), Co K-edge (c), and Fe K-edge (d). Course of Mo K-edge XANES spectra during heating (e), and corresponding LCF results using references for tetrahedral (Fe<sub>2</sub>(MoO<sub>4</sub>)<sub>3</sub>) and octahedral (MoO<sub>3</sub>) Mo coordination geometries (f). Arrows in the figures with XANES spectra point to the direction of observed changes during TPO.

neously formed. Also RS revealed the formation of  $\alpha$ -Bi<sub>2</sub>Mo<sub>3</sub>O<sub>12</sub> at  $\sim$ 460 °C and its reaction with iron oxides under formation of Bi<sub>3</sub>(-FeO<sub>4</sub>)(MoO<sub>4</sub>)<sub>2</sub> at higher temperatures (c.f. ref. [65,66]), thereby confirming the XAS results at Bi L<sub>3</sub>- and Fe K-edges. Furthermore, the presence of Fe<sub>2</sub>(MoO<sub>4</sub>)<sub>3</sub> was observed starting from 460 °C (RS) and 490 °C (XRD), respectively, and increased with increasing temperature. This indicates that amorphous or nano-crystalline Fe<sub>2</sub>O<sub>3</sub>, detectable only by XAS (c.f. ref. [63]), led to formation of Fe<sub>2</sub>(-MoO<sub>4</sub>)<sub>3</sub> in both catalysts, and furthermore reacted with  $\alpha$ -Bi<sub>2</sub>Mo<sub>3</sub>O<sub>12</sub> to form Bi<sub>3</sub>(FeO<sub>4</sub>)(MoO<sub>4</sub>)<sub>2</sub> in the case of FSP-2. Notably, for FSP-2 the crystalline phase amounts changed during the isothermal period at 600 °C, which is contrary to the phase formation behavior of FSP-1. Even though the initial phase composition of both FSP-made Bi-Mo-Co-Fe-O catalysts was similar, partially other phases (e.g., Bi<sub>3</sub>(FeO<sub>4</sub>)(MoO<sub>4</sub>)<sub>2</sub>) were formed during TPO,

highlighting the strong influence of the relative catalyst composition on the presence of metal oxide phases.

### 3.2.4. Summary on the phase evolution in Bi-Mo-Co-Fe-O catalysts during TPO

Compared to the two-component bismuth molybdate systems, many more phase transformations occurred during TPO in the two investigated four-component Bi-Mo-Co-Fe-O systems as unraveled by *in situ* TG-DSC-MS, XAS, RS, and XRD, with the different sensitivity of each technique providing complementary insights. For instance, MoO<sub>3</sub> formation during TPO of FSP-1 was only indicated by XAS but was clearly revealed by RS and XRD. An overview of the structural evolution of FSP-1 and FSP-2 during TPO is given in Fig. 6.

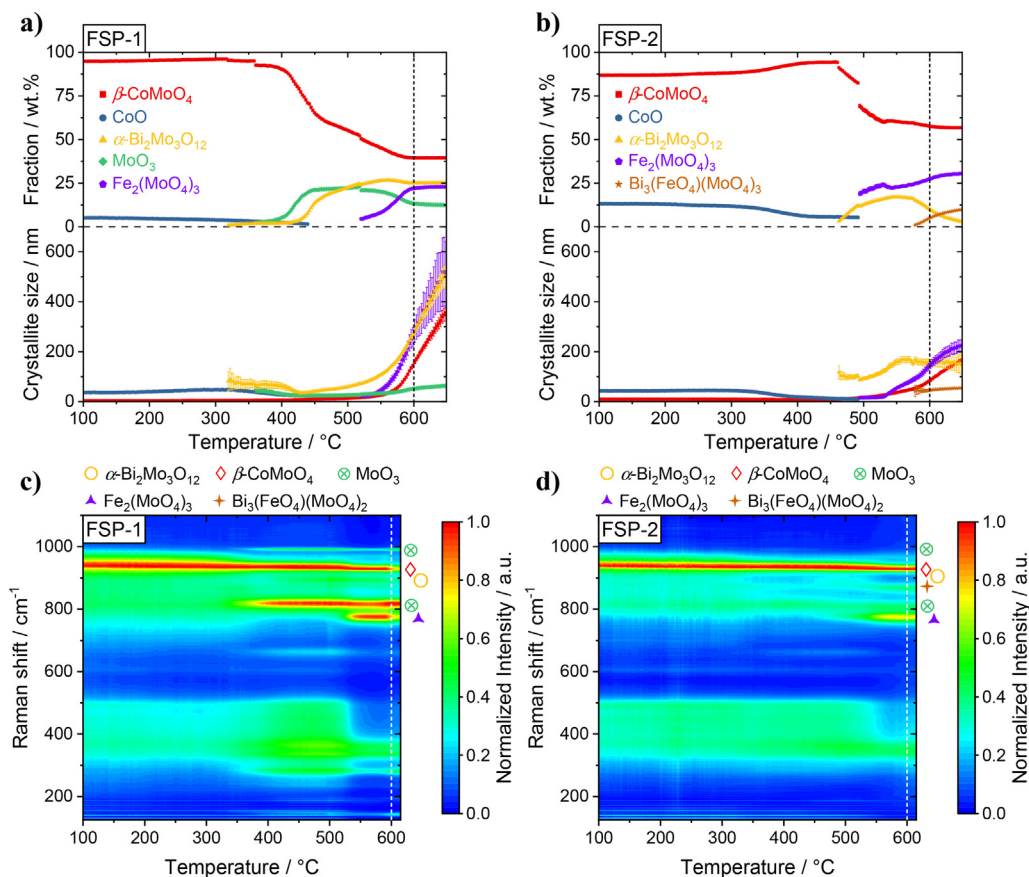


**Fig. 5.** Structural evolution of FSP-made Bi-Mo-Co-Fe-O (left: FSP-1, right: FSP-2) during TPO (100–600 °C, He/O<sub>2</sub> = 88/12 vol%) derived from XRD (a, b) and RS (c, d). Crystalline phase fractions and corresponding crystallite sizes from XRD (FSP-1: a, FSP-2: b), and normalized 2D Raman intensity plot with the assignment of metal oxide phases (FSP-1: c, FSP-2: d). Dotted vertical lines indicate the start of the isothermal period at 600 °C (10 min each).

Though similar phases were observed in both samples (e.g., Fe<sub>2</sub>(MoO<sub>4</sub>)<sub>3</sub>, α-Bi<sub>2</sub>Mo<sub>3</sub>O<sub>12</sub>), their formation and crystallization depended on temperature, confirming the TG–DSC–MS results. When all the phase analysis results (DSC, XAS, XRD, RS) are combined, an accurate understanding of phase formation, transition and crystallization processes is enabled. For instance, the DSC signals during heating of FSP-1 can thus be ascribed to discrete processes (340 °C: formation of some crystalline MoO<sub>3</sub>, 380 °C: pronounced crystallization of MoO<sub>3</sub>, 415 °C: crystallization of α-Bi<sub>2</sub>Mo<sub>3</sub>O<sub>12</sub>, 500–570 °C: formation and crystallization of Fe<sub>2</sub>(MoO<sub>4</sub>)<sub>3</sub>, >590 °C: pronounced crystal growth for all phases). However, a temperature difference is expected between DSC and XRD analysis due to the low sensitivity of XRD for the initial crystalliza-

tion of amorphous phases in these multiphase mixtures. On the other hand, RS is essential to monitor the formation of amorphous phases but might fail to identify some phases due to its limited material sensitivity.

For FSP-2, the higher Fe/Mo ratio (FSP-1 = 0.15, FSP-2 = 0.25) led to the incorporation of Fe in α-Bi<sub>2</sub>Mo<sub>3</sub>O<sub>12</sub> since not all Fe could be incorporated within Fe<sub>2</sub>(MoO<sub>4</sub>)<sub>3</sub> under oxidizing conditions. Moreover, the Co amount plays an important role in phase formation, as under oxidizing conditions it first attracts Mo as β-CoMoO<sub>4</sub>. The final amount of β-CoMoO<sub>4</sub> was significantly higher for FSP-2 (57 wt%, Co/Mo ratio = 0.67) than for FSP-1 (40 wt%, Co/Mo ratio = 0.42). As a consequence, the Co/Mo ratio also determines the amount of Mo available for other phase formation

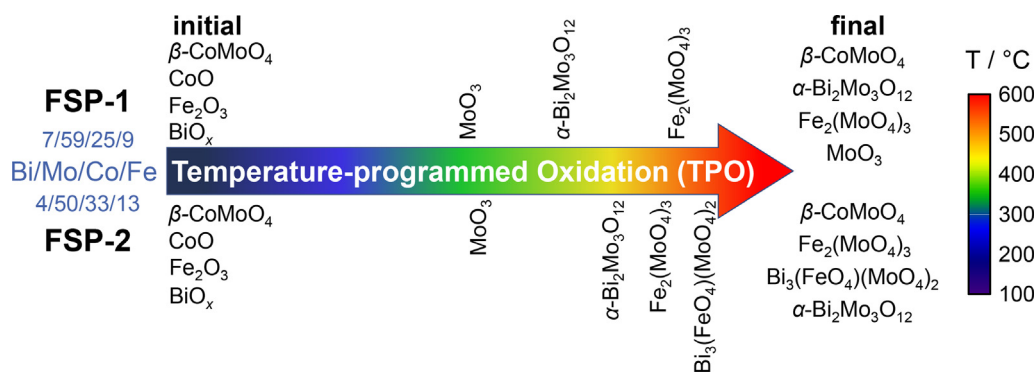


**Fig. 6.** Overview of structural evolution of FSP-made Bi-Mo-Co-Fe-O catalysts during TPO up to 600 °C.

processes. Subsequently, the Fe/Mo ratio influences the formation of binary ( $\text{Fe}_2(\text{MoO}_4)_3$ ) as well as ternary phases ( $\text{Bi}_3(\text{FeO}_4)(\text{MoO}_4)_2$ ), and thus also determines the presence of  $\text{MoO}_3$ .

### 3.3. Phase formation during TPRM

#### 3.3.1. Thermogravimetric analysis combined with mass spectrometry

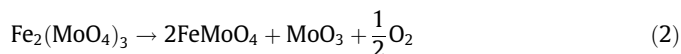
Combined TG–MS studies were carried out to follow possible reduction processes occurring under reaction conditions (e.g., to check for the (partial)  $\text{Fe}^{3+}$  to  $\text{Fe}^{2+}$  reduction which is known to occur under reaction conditions [33,42]) and to correlate them with the catalytic performance using on-line MS. Due to pronounced catalytic activity of the TG–MS setup itself under reaction conditions at higher temperatures, only datasets up to 500 °C are shown in Fig. 7. Further, the empty crucible measurement (see Figure S8b) revealed that the influence of the TG setup started at ~350 °C. Thus, the influence of the setup itself should be considered when interpreting the catalytic activity results during TG–MS experiments.

Two pronounced weight losses were observed for both catalysts during TPRM (see Fig. 7). A first loss of ~2 wt% occurred in the range of 60–200 °C and was assigned to  $\text{H}_2\text{O}$  desorption/release. A plateau was reached at ~200 °C, followed by product formation (increase of acrolein,  $\text{CO}_2$ ,  $\text{H}_2\text{O}$ ). Starting at ~270 °C, a pronounced second weight loss took place, which led to a strong increase in product formation including CO and acrylic acid. Notably, the product formation of both catalysts started at the same temperature, but FSP–2 showed a shift in the MS data inflection points of ~10 °C to lower temperature (see Figure S9 for direct comparison). For both catalysts, the inflection point for the second mass loss was at ~330 °C. Hence, the same reduction processes took place but were more pronounced in the case of FSP–2 (1.8 wt% vs. 1.4 wt% for FSP–1). This indicates a correlation between the catalyst reduction and the activity during TG–MS experiments, and thus during catalytic tests. The reduction process lasted to slightly higher temperatures for FSP–2, correlating with the more pronounced weight loss. From about 380–390 °C on, the lower rate of weight loss indicates the presence of fewer reduceable species or transport limitations. This went in hand with a lower selectivity of the catalysts due to increased formation of overoxidation products such as acrylic acid,  $\text{CO}_2$ , and CO, while the acrolein signal remained constant (FSP–1) or even decreased (FSP–2). However, at the same time the influence of the setup on the MS data has to be taken into account.

#### 3.3.2. Operando X-ray absorption spectroscopy

To investigate the influence of reaction conditions and the associated reduction observed during TG–MS on the phase formation

processes, multi-edge *operando* XAS was performed. XANES spectra at the studied metal edges for FSP–1 under isothermal conditions during TPRM together with selected reference compounds are given in Fig. 8a–d (for course see Figure S15). Similar to TPO, changes in Mo coordination were observed. However, at Fe K-edge, large changes were observed during TPRM compared to TPO. Strong reduction of Fe was uncovered with the final spectrum pointing towards complete reduction of  $\text{Fe}^{3+}$  to  $\text{Fe}^{2+}$  (Fig. 8d). As the final spectrum was close to  $\text{FeMoO}_4$  (c.f. ref. [41,64]), most likely reduction of  $\text{Fe}_2(\text{MoO}_4)_3$  to  $\text{FeMoO}_4$  occurred (see Eq. (2)).



LCF of the Mo K-edge spectra (Fig. 8e) was performed using  $\text{MoO}_3$  and  $\text{Fe}_2(\text{MoO}_4)_3$  as references for octahedral and tetrahedral coordination, respectively (see section 3.2.2). With increasing temperature, the amount of  $\text{MoO}_3$  slowly decreased from initially 42 to 36% at 315 °C. Subsequently, the amount of  $\text{MoO}_3$  temporarily increased up to 43% at ~370 °C, as also observed for oxidizing conditions (see Fig. 3f). Above 480 °C, a pronounced transition towards tetrahedral nature was observed, resulting finally in a similar state as for TPO. Furthermore, FT EXAFS fitting at Mo K-edge (see Table S13 and Figure S16) revealed an increase in the CN of Mo–O at 1.76 Å from initially 2.9 to finally 3.6, which confirms stronger tetrahedral coordination. Further, a stronger backscattering from higher shells was observed, hence indicating crystallization of Mo containing phases.

In the case of Fe K-edge XANES spectra, the first and last spectrum during heating were used for LCF (Fig. 8f) due to poor fitting results from available reference spectra. LCF analysis revealed that the main reduction occurred between 310 and 415 °C, as the amount of  $\text{Fe}^{2+}$  changed from 18 to 100%. The reduction temperature range matches the interim  $\text{MoO}_3$  formation observed at Mo K-edge, thus supporting the reaction according to Eq. (2). Furthermore, FT EXAFS fitting at Fe K-edge confirmed the reaction-induced loss of oxygen, as the CN of the Fe–O<sub>1</sub> path decreased from initially 5.2 to finally 4.5, indicative of tetrahedral  $\beta\text{-FeMoO}_4$  [41]. An increased backscattering from higher shells was also observed, indicating further crystallization. The final spectra obtained at Bi L<sub>3</sub>- (Fig. 8b) and Co K-edge (Fig. 8c) together with FT EXAFS fitting at Co K-edge (see Table S13 and Figure S16) revealed the formation of  $\alpha\text{-Bi}_2\text{Mo}_3\text{O}_{12}$  and  $\beta\text{-CoMoO}_4$ , respectively, which is similar to TPO.

The XANES spectra of FSP–2 at the studied metal edges under isothermal conditions during TPRM are shown in Fig. 9a–d together with selected references (for course see Figure S17). Similar changes were observed for Mo K-, Co K-, and Fe K-edges compared to FSP–1, including stronger tetrahedral nature for Mo, reduction of  $\text{Fe}^{3+}$  to  $\text{Fe}^{2+}$ , and formation of  $\beta\text{-CoMoO}_4$ . However,

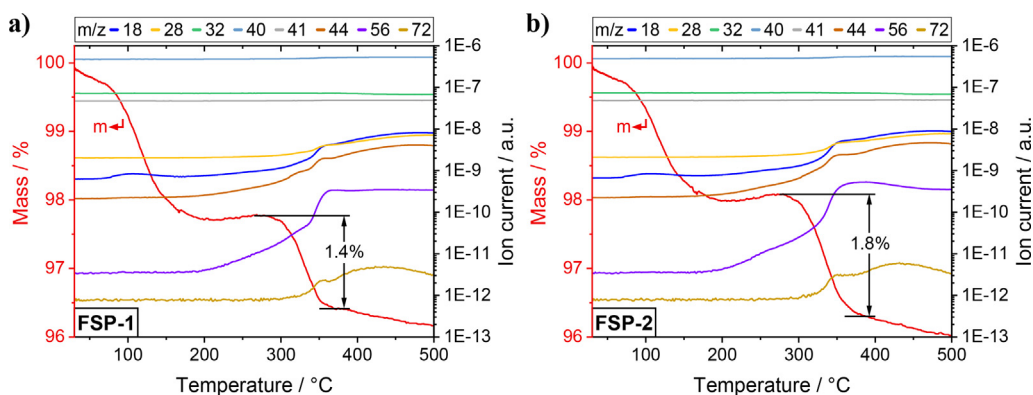
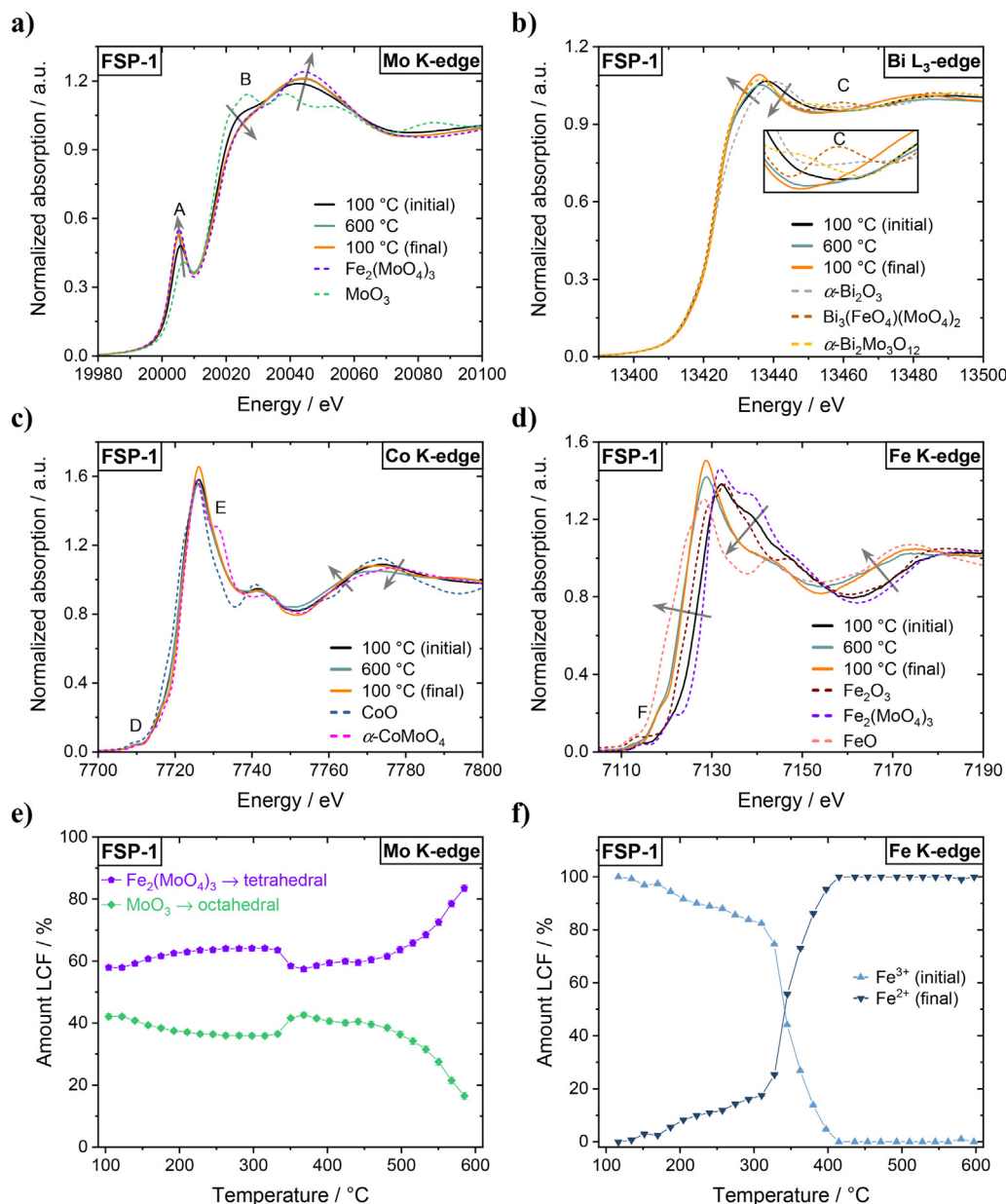


Fig. 7. Combined TG–MS data for FSP–1 (a) and FSP–2 (b) during heating under reaction conditions (25.1 mg catalyst,  $\text{Ar}/\text{O}_2/\text{C}_3\text{H}_6 = 80/12/8$  vol%; 100 mL  $\text{min}^{-1}$  total flow). Most intense MS signal for different species with  $m/z$ : 18:  $\text{H}_2\text{O}$ , 28: CO, 32:  $\text{O}_2$ , 40: Ar, 41: propylene ( $\text{C}_3\text{H}_6$ ), 44:  $\text{CO}_2$ , 56: acrolein ( $\text{C}_3\text{H}_4\text{O}$ ), 72: acrylic acid ( $\text{C}_3\text{H}_4\text{O}_2$ ).



**Fig. 8.** Multi-edge XAS data for FSP-1 during TPRM. Normalized XANES spectra for the sample under isothermal conditions and selected reference compounds (dotted lines, recorded at room temperature): Mo K-edge (a), Bi L<sub>3</sub>-edge with zoom on feature C (b), Co K-edge (c), and Fe K-edge (d). LCF results obtained at Mo K-edge spectra using references for tetrahedral ( $\text{Fe}_2(\text{MoO}_4)_3$ ) and octahedral ( $\text{MoO}_3$ ) Mo coordination geometries (e), and LCF results obtained at Fe K-edge spectra using first and last spectrum acquired during heating (f). Arrows in the figures with XANES spectra point to the direction of observed changes during TPRM.

different results were obtained at the Bi L<sub>3</sub>-edge (Fig. 9b and Figure S17), where feature C was present after TPRM revealing the formation of  $\text{Bi}_3(\text{FeO}_4)(\text{MoO}_4)_2$ . Thus, even though Fe reduction occurred, Fe was further incorporated into the  $\alpha\text{-Bi}_2\text{Mo}_3\text{O}_{12}$  structure [67]. However, the amount of  $\text{Bi}_3(\text{FeO}_4)(\text{MoO}_4)_2$  phase was low as evident from the almost identical nature of Fe K-edge XANES spectra for FSP-1 and FSP-2 (see Figure S19). Fe K-edge FT EXAFS fitting (see Table S14 and Figure S18) including paths from  $\beta\text{-Co}_{0.7}\text{Fe}_{0.3}\text{MoO}_4$  revealed decreased oxygen coordination in the first shell together with a higher bond distance for the final state, supporting the XANES results.

Under reaction conditions, LCF revealed differences in Mo coordination behavior (Fig. 9e) compared to FSP-1. Between 315 and 420 °C, the amount of  $\text{MoO}_3$  decreased from 32 to 25%. As  $\text{MoO}_3$  is formed via the reduction of  $\text{Fe}^{3+}$  to  $\text{Fe}^{2+}$  (see Eq. (2)), it could be incorporated in a tetrahedrally coordinated molybdate structure

(e.g.,  $\beta\text{-FeMoO}_4$ ,  $\beta\text{-Co}_{0.7}\text{Fe}_{0.3}\text{MoO}_4$ ). As the main changes in oxidation state occurred between 310 and 415 °C (from 20 to 93%  $\text{Fe}^{2+}$ , see Fig. 9f), the Fe reduction proceeded similar to FSP-1. Since TG-MS revealed a pronounced influence of the reduction process on the catalytic activity, a detailed comparison of the reduction process and simultaneously measured catalytic activity during *operando* XAS measurements is given in Fig. 10. For higher temperatures ( $T > 500$  °C), the influence of the dilutant  $\alpha\text{-Al}_2\text{O}_3$  (see Figure S20) should be kept in mind when evaluating the MS data during activation.

The Fe reduction rate (Fig. 10a bottom), which was derived from the reduction progress (Fig. 10a top) and corrected by the Fe amount (see Table 1), was highest at  $\sim 345$  °C for both samples. However, in the case of FSP-2 the reduction started at slightly lower temperatures and lasted up to higher temperatures, what can be explained by the higher Fe amount present. The correlation

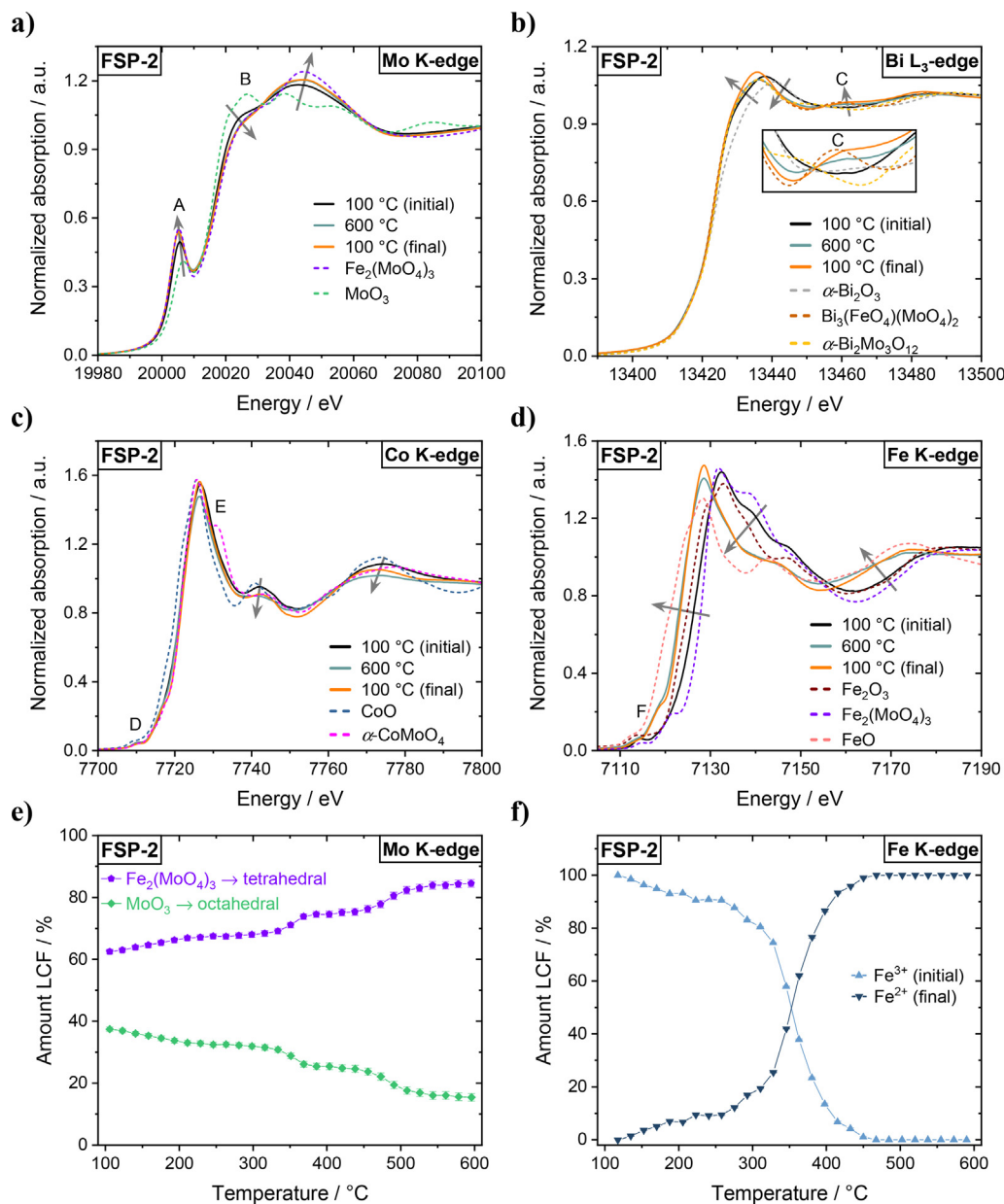


**Fig. 9.** Multi-edge XAS data for FSP-2 during TPRM. Normalized XANES spectra for the sample under isothermal conditions and selected reference compounds (dotted lines, recorded at room temperature): Mo K-edge (a), Bi L<sub>3</sub>-edge with zoom on feature C (b), Co K-edge (c), and Fe K-edge (d). LCF results obtained at Mo K-edge spectra using references for tetrahedral ( $\text{Fe}_2(\text{MoO}_4)_3$ ) and octahedral ( $\text{MoO}_3$ ) Mo coordination geometries (e), and LCF results obtained at Fe K-edge spectra using first and last spectrum acquired during heating (f). Arrows in the figures with XANES spectra point to the direction of observed changes during TPRM.

between catalyst reduction and activity, which was already observed during TG–MS studies (Fig. 7), could be confirmed and traced back to the reduction of Fe. The earlier reduction of  $\text{Fe}^{3+}$  to  $\text{Fe}^{2+}$  for FSP-2 resulted in earlier product formation, while the higher amount of Fe present in FSP-2 led to higher activity (see Fig. 10b).

In summary, multi-edge XAS revealed several phase transformations during activation of the as-prepared catalysts. In particular, reduction of  $\text{Fe}^{3+}$  to  $\text{Fe}^{2+}$  led to increased activity. Co (mainly present as  $\beta\text{-CoMoO}_4/\beta\text{-Co}_{0.7}\text{Fe}_{0.3}\text{MoO}_4$ ) and Fe (mainly present as  $\beta\text{-FeMoO}_4/\beta\text{-Co}_{0.7}\text{Fe}_{0.3}\text{MoO}_4$ ) formed similar phases, though incorporation of Mo and Bi differed between the samples. Similar to TPO, the formation of ternary phase  $\text{Bi}_3(\text{FeO}_4)(\text{MoO}_4)_2$  was only observed for FSP-2. Furthermore, FSP-1 showed a unique interim

increase in octahedral Mo coordination and thus the (interim) formation of  $\text{MoO}_3$  associated with the reduction of Fe, while for FSP-2 the released  $\text{MoO}_3$  could be bound within tetrahedrally coordinated Mo phases. Additionally, the comparison of both samples revealed that the activity correlates with Fe amount and  $\text{Fe}^{3+}$  to  $\text{Fe}^{2+}$  reduction behavior. To further analyze the phase behavior, XRD and RS experiments were conducted under reaction conditions.

### 3.3.3. Operando X-ray diffraction and Raman spectroscopy

Corresponding results for XRD and RS analysis for FSP-1 and FSP-2 are given in Fig. 11. During heating under reaction conditions of FSP-1 (Fig. 11a, c, e), partially different phases were formed compared to TPO. While for oxidizing conditions  $\text{Fe}_2(\text{MoO}_4)_3$  was observed by XAS, XRD and RS, this was not the case

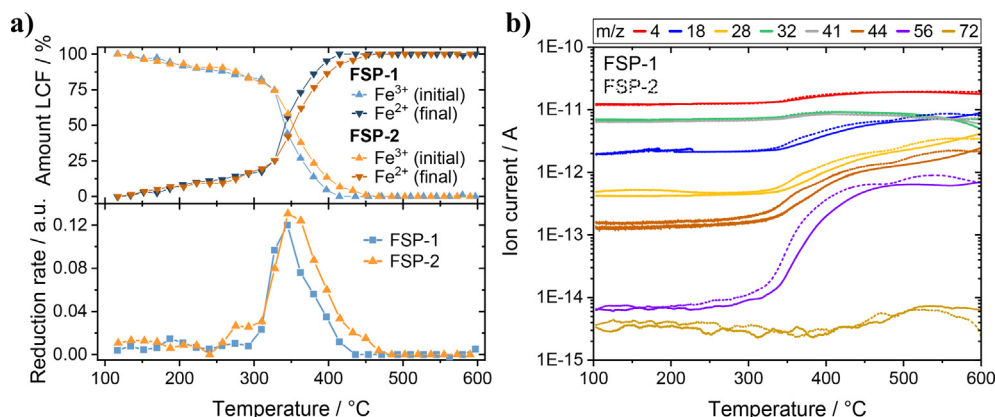


**Fig. 10.** Direct comparison of Fe K-edge LCF results (see Fig. 8f and Fig. 9f) using in each case the first and last spectrum during heating under reaction conditions as references (a, top), and Fe amount corrected reduction rates (a, bottom). Overlay of acquired MS data for FSP-1 (solid lines) and FSP-2 (dotted lines) during TPRM (b). Most intense MS signal for different species with  $m/z$ : 4: He, 18:  $\text{H}_2\text{O}$ , 28: CO, 32:  $\text{O}_2$ , 41: propylene ( $\text{C}_3\text{H}_6$ ), 44:  $\text{CO}_2$ , 56: acrolein ( $\text{C}_3\text{H}_4\text{O}$ ), 72: acrylic acid ( $\text{C}_3\text{H}_4\text{O}_2$ ). The MS signals for acrolein and acrylic acid were smoothed due to high level of noise for low ion currents.

for reaction conditions. Furthermore, no  $\text{FeMoO}_4$  phase could be observed by XRD nor RS and no other Fe containing phases were detected. Hence, it is very likely that  $\beta\text{-Co}_{0.7}\text{Fe}_{0.3}\text{MoO}_4$  was formed during TPRM. Thus,  $\beta\text{-Co}_{0.7}\text{Fe}_{0.3}\text{MoO}_4$  instead of  $\beta\text{-CoMoO}_4$  was used for Rietveld refinement of the obtained XRD patterns. However, it should be noted that due to the similar structures of both compounds, it was not possible to unambiguously distinguish these by XRD within the complex phase mixture present. Therefore, only one structure was used for the refinement of an entire TPRM cycle, even though the Fe incorporation into the  $\beta\text{-CoMoO}_4$  structure might have occurred at higher temperatures as indicated by an increased phase amount above  $550^\circ\text{C}$  (Fig. 11a).

For completeness, Rietveld refinement was also carried out using  $\beta\text{-CoMoO}_4$  but resulted in higher  $R_{\text{wp}}$  values (especially for higher temperatures) indicating a worse refinement (see Figure S31). Furthermore, the absence of other Fe containing phases supports the assumption of  $\beta\text{-Co}_{0.7}\text{Fe}_{0.3}\text{MoO}_4$  formation in combination with the better refinements when using this structure.

Notably, the final state of FSP-1 consisted only of  $\beta\text{-Co}_{0.7}\text{Fe}_{0.3}\text{MoO}_4$ ,  $\alpha\text{-Bi}_2\text{Mo}_3\text{O}_{12}$  and  $\text{MoO}_3$ , which were formed during TPRM. A drastic increase in crystalline  $\text{MoO}_3$  amount took place from  $400$  to  $465^\circ\text{C}$  (Fig. 11a), while the  $\alpha\text{-Bi}_2\text{Mo}_3\text{O}_{12}$  amount increased between  $450$  and  $480^\circ\text{C}$ , both at the expense of  $\beta\text{-Co}_{0.7}\text{Fe}_{0.3}\text{MoO}_4$ . Additionally, the observed increase in  $\beta\text{-Co}_{0.7}\text{Fe}_{0.3}\text{MoO}_4$  amount above  $550^\circ\text{C}$  is in line with a decrease in crystalline  $\text{MoO}_3$  amount, which further supports formation of  $\beta\text{-Co}_{0.7}\text{Fe}_{0.3}\text{MoO}_4$  from  $\beta\text{-CoMoO}_4$ ,  $\text{MoO}_3$  and amorphous Fe compounds (e.g.,  $\text{FeO}$ ,  $\text{Fe}_2\text{O}_3$ ) according to Eq. (3).



However, a decrease in  $\text{MoO}_3$  amount for temperatures above  $550^\circ\text{C}$  could not be confirmed by RS. This might be affected by different Raman scattering properties of  $\beta\text{-CoMoO}_4$  and  $\beta\text{-Co}_{0.7}\text{Fe}_{0.3}\text{MoO}_4$ , respectively. Since  $\text{MoO}_3$  is a strong Raman scatterer, amorphous  $\text{MoO}_3$  was already observed at  $\sim 330^\circ\text{C}$ , which matches well the  $\text{MoO}_3$  formation and Fe reduction process revealed by XAS (see Fig. 8e–f). As monitored by MS (Fig. 11e), the release or formation of  $\text{MoO}_3$  during the catalyst reduction led to an interim plateau in acrolein formation at  $330\text{--}345^\circ\text{C}$  while formation of by-products like CO and  $\text{CO}_2$  was further increasing. Notably, especially  $\text{CO}_2$  was formed as indicated by the rather high ion current for  $m/z = 44$  (Fig. 11e). In the temperature range  $370\text{--}410^\circ\text{C}$ , a second, more pronounced effect of  $\text{MoO}_3$  formation/crystallization was observed as the intensity ratio of Raman bands associated to  $\text{MoO}_3$  compared to  $\beta\text{-Co}_{0.7}\text{Fe}_{0.3}\text{MoO}_4$  was changing significantly

(see Fig. 11c and Figure S25) and crystalline  $\text{MoO}_3$  formed (see Fig. 11a). Notably, propylene conversion did not follow the trend of increasing activity with increasing temperature in this temperature range as it remained almost constant and only increased later on ( $T > 410^\circ\text{C}$ ). This indicates that (crystalline)  $\text{MoO}_3$  does not contribute in a beneficial manner to catalytic activity of Bi–Mo–Co–Fe–O systems.

The structural changes during TPRM for FSP-2 are shown in Fig. 11b, d, f. As for FSP-1, the Rietveld refinement results for  $\beta\text{-CoMoO}_4$  as main phase are given in Figure S31. According to Rietveld refinement (Fig. 11b) and RS (Fig. 11d), the phase formation processes for FSP-2 differed significantly compared to TPO conditions and also compared to FSP-1 under TPRM conditions. In addition to the initially present  $\beta\text{-CoMoO}_4/\beta\text{-Co}_{0.7}\text{Fe}_{0.3}\text{MoO}_4$  and CoO, phases including  $\text{MoO}_3$ ,  $\alpha\text{-Bi}_2\text{Mo}_3\text{O}_{12}$  and  $\text{Bi}_3(\text{FeO}_4)(\text{MoO}_4)_2$  formed during TPRM. First,  $\text{MoO}_3$  was formed as revealed by RS ( $330^\circ\text{C}$ ) and XRD ( $380^\circ\text{C}$ ). Similarly to FSP-1, amorphous  $\text{MoO}_3$  occurred together with the reduction of Fe. Nevertheless,  $\text{MoO}_3$  was only present as an interim phase in the case of FSP-2, as the corresponding signals disappeared above  $535^\circ\text{C}$  (RS) and  $565^\circ\text{C}$  (XRD). The observed temperature difference might originate from different heating rates in both experiments (XRD:  $5^\circ\text{C min}^{-1}$ , RS:  $1.5^\circ\text{C min}^{-1}$ ). Since the crystalline amount of  $\beta\text{-Co}_{0.7}\text{Fe}_{0.3}\text{MoO}_4$  increased from  $\sim 480^\circ\text{C}$  on, it was likely formed according to Eq. (3). The final amount of  $\beta\text{-Co}_{0.7}\text{Fe}_{0.3}\text{MoO}_4$  was  $\sim 85\text{ wt}\%$ , which is far higher compared to FSP-1 ( $59\text{ wt}\%$ ), but can be traced back to the higher Co/Mo and Fe/Mo ratios in FSP-2 (see Table 1). Furthermore,  $\text{Bi}_3(\text{FeO}_4)(\text{MoO}_4)_2$  was observed by XRD and especially RS. Thus, also under partly reducing conditions, Fe could be incorporated into the  $\alpha\text{-Bi}_2\text{Mo}_3\text{O}_{12}$  structure forming the scheelite structured  $\text{Bi}_3(\text{FeO}_4)(\text{MoO}_4)_2$  phase [67], confirming the XAS results (see Fig. 9b).

Since the formation of  $\beta\text{-Co}_{0.7}\text{Fe}_{0.3}\text{MoO}_4$  occurred at lower temperatures compared to the formation of  $\text{Bi}_3(\text{FeO}_4)(\text{MoO}_4)_2$ , it can be concluded that not all Fe oxides could be incorporated into the  $\beta\text{-CoMoO}_4$  structure, and thus were still available for the formation of  $\text{Bi}_3(\text{FeO}_4)(\text{MoO}_4)_2$ . The limiting factor for the Fe incorporation into  $\beta\text{-CoMoO}_4$  was most probably the amount of available  $\text{MoO}_3$  (Eq. (3)), which was influenced by the initial catalyst composition.

In the temperature range  $330\text{--}400^\circ\text{C}$ , FSP-2 exhibited high selectivity towards CO and  $\text{CO}_2$  compared to acrolein as shown in Fig. 11f. In this temperature range, RS revealed the most pronounced changes in relative phase composition (Fig. 11d), as the amount of  $\text{MoO}_3$  strongly increased, which was confirmed by XRD. Moreover, the disappearance of  $\text{MoO}_3$  caused by its incorpo-

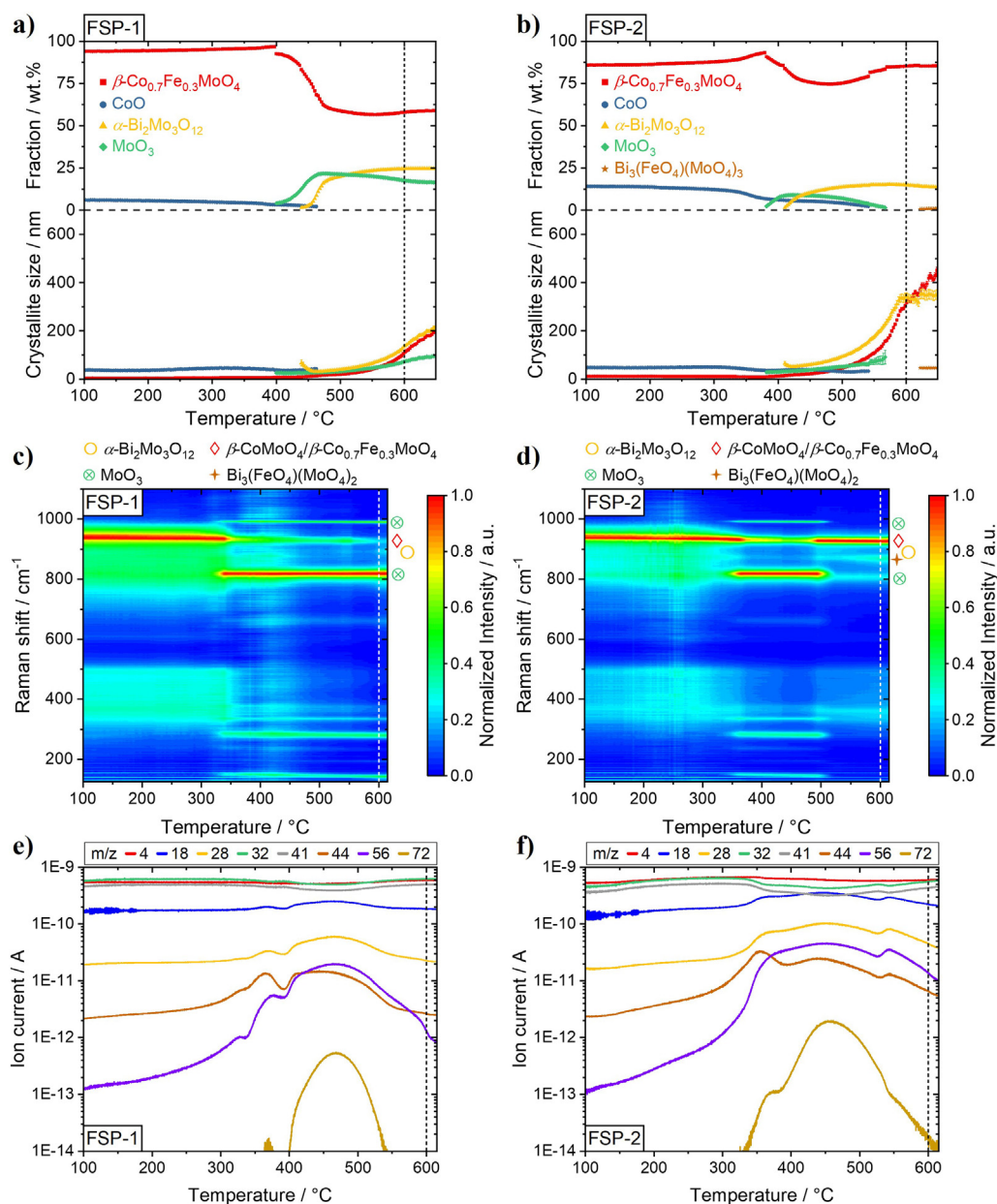


**Fig. 11.** Structural evolution of FSP-made Bi–Mo–Co–Fe–O (left: FSP–1, right: FSP–2) during TPRM (100–600 °C, He/O<sub>2</sub>/C<sub>3</sub>H<sub>6</sub>/H<sub>2</sub>O = 72/12/8/8 vol%) derived from XRD (a, b) and RS (c, d) together with MS data (e, f). Crystalline phase fractions and corresponding crystallite sizes from XRD (FSP–1: a, FSP–2: b), normalized 2D Raman intensity plot with the assignment of metal oxide phases (FSP–1: c, FSP–2: d), and mass spectroscopic data acquired during Raman spectroscopic studies (FSP–1: e, FSP–2: f). Most intense MS signal for different species with *m/z*: 4: He, 18: H<sub>2</sub>O, 28: CO, 32: O<sub>2</sub>, 41: propylene (C<sub>3</sub>H<sub>6</sub>), 44: CO<sub>2</sub>, 56: acrolein (C<sub>3</sub>H<sub>4</sub>O), 72: acrylic acid (C<sub>3</sub>H<sub>4</sub>O<sub>2</sub>). Dotted vertical lines indicate the start of the isothermal period at 600 °C (10 min each).

ration into  $\beta$ -CoMoO<sub>4</sub> together with amorphous Fe compounds forming  $\beta$ -Co<sub>0.7</sub>Fe<sub>0.3</sub>MoO<sub>4</sub> (Eq. (3)) at ~535 °C led to a strong increase in performance. Not only propylene conversion increased but also the increase in the ion current of acrolein was more pronounced compared to the increase in by-products like CO and CO<sub>2</sub>. Thus, it can be concluded that MoO<sub>3</sub> acts as unselective phase in propylene oxidation to acrolein, at least in Bi–Mo–Co–Fe–O catalysts. This is also in line with the findings of Udalova *et al.* [39] for Co–Mo–Bi–Fe–Sb–K catalysts.

Furthermore, our results support the promoting effect of  $\beta$ -Co<sub>0.7</sub>Fe<sub>0.3</sub>MoO<sub>4</sub>, which was already described for mixtures of bismuth molybdates and mixed cobalt iron molybdates. The synergy effect between these metal oxide phases was traced back to facilitated electron and oxygen ion mobility when they are in close

contact, and thus the increased efficiency of the redox mechanism according to the Mars–van Krevelen mechanism [25,26,37,68]. The higher amount of  $\beta$ -Co<sub>0.7</sub>Fe<sub>0.3</sub>MoO<sub>4</sub> in FSP–2 is most likely one origin for the better performance compared to FSP–1, which was also observed by MS during the *operando* Raman spectroscopic studies (see Figure S29). Such a trend is in line with the screening results of Millet *et al.* [26] under variation of the  $\beta$ -Co<sub>0.7</sub>Fe<sub>0.3</sub>MoO<sub>4</sub>/ $\alpha$ -Bi<sub>2</sub>Mo<sub>3</sub>O<sub>12</sub> ratio showing that only a rather low  $\alpha$ -Bi<sub>2</sub>Mo<sub>3</sub>O<sub>12</sub> amount is required for high activity and acrolein selectivity although  $\alpha$ -Bi<sub>2</sub>Mo<sub>3</sub>O<sub>12</sub> is ascribed the active phase.

### 3.3.4. Summary on the phase evolution in Bi–Mo–Co–Fe–O catalysts during TPRM and the influence on catalytic performance

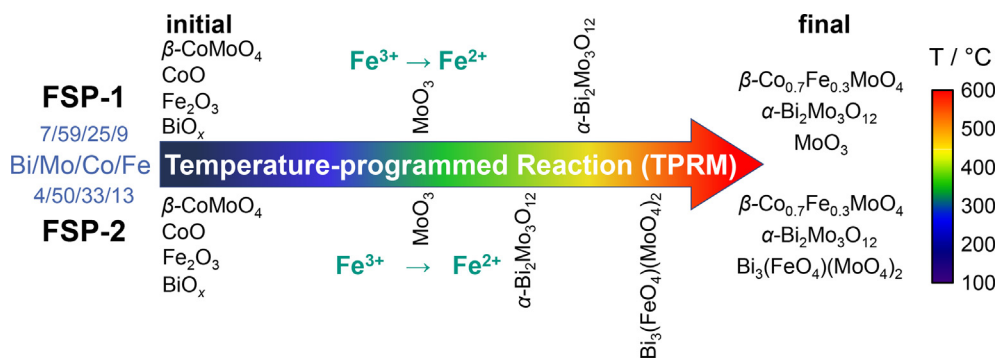


Fig. 12. Overview of structural evolution of FSP-made Bi-Mo-Co-Fe-O catalysts during TPRM up to 600 °C.

During the course of TPRM, the reduction of  $\text{Fe}^{3+}$  to  $\text{Fe}^{2+}$  was observed for both samples. This reduction led to a strong increase in catalytic performance linked to formation of different phases compared to TPO. As shown in Fig. 12, the final composition of FSP-1 after TPRM was made up by  $\beta\text{-Co}_{0.7}\text{Fe}_{0.3}\text{MoO}_4$ ,  $\alpha\text{-Bi}_2\text{Mo}_3\text{O}_{12}$ , and  $\text{MoO}_3$  (TPO:  $\beta\text{-CoMoO}_4$ ,  $\alpha\text{-Bi}_2\text{Mo}_3\text{O}_{12}$ ,  $\text{Fe}_2(\text{MoO}_4)_3$ ,  $\text{MoO}_3$ ), while FSP-2 finally consisted of  $\beta\text{-Co}_{0.7}\text{Fe}_{0.3}\text{MoO}_4$ ,  $\alpha\text{-Bi}_2\text{Mo}_3\text{O}_{12}$ , and  $\text{Bi}_3(\text{FeO}_4)(\text{MoO}_4)_2$  (TPO:  $\beta\text{-CoMoO}_4$ ,  $\alpha\text{-Bi}_2\text{Mo}_3\text{O}_{12}$ ,  $\text{Fe}_2(\text{MoO}_4)_3$ ,  $\text{Bi}_3(\text{FeO}_4)(\text{MoO}_4)_2$ ).

It is reported that the reduction of  $\text{Fe}^{3+}$  to  $\text{Fe}^{2+}$ , and thus the  $\text{Fe}^{3+}/\text{Fe}^{2+}$  redox couple, strongly depends on the presence of metal oxide phases. While  $\text{CoMoO}_4$  can stabilize  $\text{Fe}^{2+}$  within the mixed  $\text{Co}_x\text{Fe}_{1-x}\text{MoO}_4$  phase,  $\alpha\text{-Bi}_2\text{Mo}_3\text{O}_{12}$  can stabilize  $\text{Fe}^{3+}$  [27,35]. Notably, we did not observe the formation of  $\text{Fe}_2(\text{MoO}_4)_3$  under reaction conditions. However, this might be influenced by the elemental catalyst composition as well as by the gas composition as the amount of  $\text{O}_2$  in the gas feed has an influence on the  $\text{Fe}^{3+}/\text{Fe}^{2+}$  redox couple [27]. In general, our results on the activation of Bi-Mo-Co-Fe-O catalysts underline that more metal oxide phases than the typically investigated phases  $\text{Co}_x\text{Fe}_{1-x}\text{MoO}_4$  and  $\alpha\text{-Bi}_2\text{Mo}_3\text{O}_{12}$  [25,26,35,37] need to be considered when studying the phase cooperation of Bi-Mo-Co-Fe-O systems.

As the individual phase composition of both catalysts after TPRM is similar to the state after catalytic testing (see Fig. 1), the *operando* experiments revealed the various processes taking place during transition from the as-prepared to the active state. In general, preferentially binary and ternary metal oxides were formed. However, the relative catalyst composition (*i.e.*, metal ratios) had a strong influence on phase composition in the active state and thus catalytic performance. In the case of FSP-1, not all  $\text{MoO}_3$ , which acts as unselective phase, could react to form binary or ternary metal oxide phases due to the high Mo amount ( $\text{Mo}/(\text{Co} + \text{Fe})$  ratio = 1.76). For FSP-2 ( $\text{Mo}/(\text{Co} + \text{Fe})$  ratio = 1.09), all free  $\text{MoO}_3$  was incorporated in  $\beta\text{-Co}_{0.7}\text{Fe}_{0.3}\text{MoO}_4$ .

On one hand,  $\text{MoO}_3$  is inevitably formed during reduction of the as-prepared catalysts and subsequently binds free oxides that also act as unselective components (*e.g.*, iron oxides [38]). Thus, a certain  $\text{MoO}_3$  amount is required to obtain a well performing catalyst. On the other hand, an excess of  $\text{MoO}_3$  decreases the catalytic performance as in the case of FSP-1. These findings confirm the results of Udalova *et al.* [39] for Co-Mo-Bi-Fe-Sb-K catalysts. However, it should be noted that not only  $\text{MoO}_3$  binds free oxides forming binary metal molybdates (*e.g.*,  $\text{CoMoO}_4$ ,  $\text{FeMoO}_4$ ), but also binary phases can bind free oxides forming ternary metal oxide phases (*e.g.*,  $\beta\text{-Co}_{0.7}\text{Fe}_{0.3}\text{MoO}_4$ ,  $\text{Bi}_3(\text{FeO}_4)(\text{MoO}_4)_2$ ). The formation of these ternary metal oxides and their synergistic interaction with  $\alpha\text{-Bi}_2\text{Mo}_3\text{O}_{12}$  appear to be responsible for the outstanding performance of FSP-2 compared to FSP-1. Notably, their sole presence is not sufficient if there is no mutual interaction between them, which might be influenced by the preparation technique. For instance,

$\text{Bi}_3(\text{FeO}_4)(\text{MoO}_4)_2$  alone does not exhibit a higher activity than bismuth molybdates [69,70], but if it is in contact with bismuth molybdates and iron molybdates a pronounced performance increase can be observed [38,71].

The results shown here highlight the need to investigate real multicomponent catalysts, with both complex structure and intermixed phases. This is in contrast to rather simplified systems or phase mixtures which are often studied in literature but may not be representative of a real catalyst at work. *Operando* characterization is crucial to cover all relevant phases forming on stream and thus their interaction, which can help to rationalize the outstanding performance of such multicomponent catalysts compared to simplified model systems. Furthermore, a combination of complementary characterization tools is essential to compensate for the limitations in any individual method.

#### 4. Conclusions

The manifold structural changes of two FSP-made Bi-Mo-Co-Fe-O catalysts during TPO and TPRM were monitored by complementary *in situ* and *operando* multi-edge XAS, synchrotron XRD combined with Rietveld refinement, RS, and TG-DSC-MS. Both catalysts underwent strong structural changes depending on relative elemental composition, applied temperature and gas atmosphere. Synchrotron-based methods are especially ideal for such multicomponent systems as XAS can monitor local structural changes of each element (Bi, Mo, Co, Fe) independently, while XRD allows to uncover the complex crystalline phase composition. Under oxidizing conditions (TPO) preferentially binary metal oxides (*e.g.*,  $\beta\text{-CoMoO}_4$ ,  $\alpha\text{-Bi}_2\text{Mo}_3\text{O}_{12}$ ,  $\text{Fe}_2(\text{MoO}_4)_3$ ) were formed. However, the occurrence of  $\text{MoO}_3$  and  $\text{Bi}_3(\text{FeO}_4)(\text{MoO}_4)_2$  was influenced by the relative elemental composition.

For *operando* investigations under reaction conditions (TPRM), the phase formation processes differed significantly based on the reduction of  $\text{Fe}^{3+}$  to  $\text{Fe}^{2+}$  and its preferential incorporation into  $\beta\text{-CoMoO}_4$  forming  $\beta\text{-Co}_{0.7}\text{Fe}_{0.3}\text{MoO}_4$ . In general, the presence of ternary  $\text{Co}_x\text{Fe}_{1-x}\text{MoO}_4$  appears to play a key role for the better performance of Bi-Mo-Co-Fe-O compared to Bi-Mo-O systems, thereby confirming studies on simplified model systems (*i.e.*, mixtures of  $\alpha\text{-Bi}_2\text{Mo}_3\text{O}_{12}$  and  $\text{Co}_x\text{Fe}_{1-x}\text{MoO}_4$ ). Although Fe reduction led to a performance increase, the associated and inevitable formation of  $\text{MoO}_3$  lowered acrolein formation. A further performance increase occurred only if all  $\text{MoO}_3$  subsequently reacted forming other phases. This highlights the unselective role of  $\text{MoO}_3$  within the investigated systems. However,  $\text{MoO}_3$  still played a crucial role in the phase formation processes by binding other free oxides as binary (TPO) or ternary (TPRM) metal oxide phases.

Finally, the comparison of both catalysts revealed that the formation of ternary  $\beta\text{-Co}_{0.7}\text{Fe}_{0.3}\text{MoO}_4$  and  $\text{Bi}_3(\text{FeO}_4)(\text{MoO}_4)_2$  under

reaction conditions and their synergistic interplay with  $\alpha$ -Bi<sub>2</sub>Mo<sub>3</sub>O<sub>12</sub> are required for an outstanding performance (FSP-2). This supports the earlier particle models of interacting phases but extends them at the same time by unravelling the phase formation processes during catalyst activation. Moreover, it is demonstrated that more metal oxide phases than suggested in these models need to be considered for Bi–Mo–Co–Fe–O catalysts.

The multimodal approach applied here enabled detailed *operando* insights into the various phase formation/transition processes in multicomponent Bi–Mo–Co–Fe–O catalysts and their influence on the performance in selective oxidation of propylene to acrolein. The combination of complementary *operando* techniques was essential for gaining insights into structure–activity/selectivity correlations within such complex catalyst systems. In future, these emerging *operando* techniques will provide new possibilities for studying multicomponent mixed metal oxide systems and the cooperation of phases therein, which is crucial in understanding the origin of high performance compared to two–component systems.

### Author contributions

**Matthias Stehle:** Methodology, Validation, Formal analysis, Investigation, Writing – original draft, Writing – review & editing, Visualization, Project administration. **Abhijeet Gaur:** Methodology, Investigation, Formal analysis, Writing – review & editing. **Sebastian Weber:** Validation, Methodology, Formal analysis, Writing – review & editing. **Thomas Sheppard:** Conceptualization, Writing – review & editing, Supervision, Project administration. **Michael Thomann:** Conceptualization, Resources, Writing – review & editing, Supervision. **Achim Fischer:** Conceptualization, Resources, Writing – review & editing, Supervision, Funding acquisition. **Jan-Dierk Grunwaldt:** Conceptualization, Resources, Writing – review & editing, Supervision, Project administration, Funding acquisition.

### Declaration of Competing Interest

The authors declare that they have no known competing financial interests or personal relationships that could have appeared to influence the work reported in this paper.

### Acknowledgement

We acknowledge SOLEIL for provision of synchrotron radiation facilities and we would like to thank Dr. Camille La Fontaine for assistance in using beamline ROCK (proposal 20190094). The work at ROCK was supported by a public grant overseen by the French National Research Agency (ANR) as part of the “Investissements d’Avenir” program (reference: ANR10–EQPX45). The corresponding research leading to this result has been supported by the project CALIPSOplus under the Grant Agreement 730872 from the EU Framework Program for Research and Innovation HORIZON 2020. We acknowledge the European Synchrotron Radiation Facility for provision of synchrotron radiation facilities and we would like to thank Dr. Vadim Diadkin and Dr. Wouter van Beek for assistance in using beamline BM01 (proposal MA–4036). We thank the ESRF for financial support during travelling and accommodation. We acknowledge KIT and DFG for financing the Raman spectrometer system (INST 121384/73–1) and the thermogravimetric setup (INST 121384/70–1). We thank Daniel Eggart, Linda Klag, Dr. Oliver Schade, and Dr. Marc–André Serrer for assistance during beam-times as well as Ulrich Klehm (Evonik Technology & Infrastructure GmbH) for TEM–EDX measurements, Dr. Thomas Bergfeldt and Pirimze Khelashvili (IAM–AWP, KIT) for ICP–OES analysis, and Angela Deutsch (ITCP, KIT) for BET surface area experiments.

### Appendix A. Supplementary material

Supplementary data to this article can be found online at <https://doi.org/10.1016/j.jcat.2021.08.053>.

### References

- [1] J. Haber, Fundamentals of hydrocarbon oxidation, in: G. Ertl, H. Knözinger, F. Schüth, J. Weitkamp (Eds.), Handbook of Heterogeneous Catalysis, Wiley–VCH, Weinheim, 2008, pp. 3359–3384.
- [2] R.K. Grasselli, J.D. Burrington, Oxidation of Low-Molecular-Weight Hydrocarbons, in: G. Ertl, H. Knözinger, F. Schüth, J. Weitkamp (Eds.), Handbook of Heterogeneous Catalysis, Wiley–VCH, Weinheim, 2008, pp. 3479–3489.
- [3] G. Centi, F. Cavani, F. Trifirò, in: Trends and Outlook in Selective Oxidation, in: Selective Oxidation by Heterogeneous Catalysis, Springer, Boston, MA, 2001, pp. 1–24.
- [4] Teles, J.H., Hermans, I., Franz, G., Sheldon, R.A., Oxidation, in: Ullmann’s Encyclopedia of Industrial Chemistry, Wiley–VCH, Weinheim, 2015, pp. 1–103. [https://doi.org/10.1002/14356007.a18\\_261.pub2](https://doi.org/10.1002/14356007.a18_261.pub2).
- [5] P. Sprenger, W. Kleist, J.–D. Grunwaldt, Recent Advances in Selective Propylene Oxidation over Bismuth Molybdate Based Catalysts: Synthetic, Spectroscopic, and Theoretical Approaches, ACS Catal. 7 (2017) 5628–5642.
- [6] Arntz, D., Fischer, A., Höpp, M., Jacobi, S., Sauer, J., Ohara, T., Sato, T., Shimizu, N., Schwind, H. Acrolein and methacrolein, in: Ullmann’s encyclopedia of industrial chemistry, Wiley–VCH, Weinheim, 2007, pp. 329–346. [https://doi.org/10.1002/14356007.a01\\_149.pub2](https://doi.org/10.1002/14356007.a01_149.pub2).
- [7] R.K. Grasselli, Site isolation and phase cooperation: Two important concepts in selective oxidation catalysis: A retrospective, Catal. Today 238 (2014) 10–27. [https://doi.org/10.1002/14356007.a01\\_149.pub2](https://doi.org/10.1002/14356007.a01_149.pub2).
- [8] Y. Moro-Oka, W. Ueda, Multicomponent bismuth molybdate catalyst: A highly functionalized catalyst system for the selective oxidation of olefin, Adv. Catal. 40 (1994) 233–273.
- [9] L. Liu, X.P. Ye, J.J. Bozell, A Comparative Review of Petroleum-Based and Bio-Based Acrolein Production, ChemSusChem 5 (7) (2012) 1162–1180.
- [10] D. Carson, G. Coudurier, M. Forissier, J.C. Védrine, A. Laarif, F. Theobald, Synergy effects in the catalytic properties of bismuth molybdates, J. Chem. Soc., Faraday Trans. 1 (79) (1983) 1921–1929.
- [11] Z. Bing, S. Pei, S. Shishan, G. Xiexian, Cooperation between the  $\alpha$  and  $\gamma$  phases of bismuth molybdate in the selective oxidation of propene, J. Chem. Soc., Faraday Trans. 86 (1990) 3145–3150.
- [12] L.M. Thang, I. van Driessche, Catalytic Activities of  $\alpha$ ,  $\beta$ ,  $\gamma$ -Bismuth Molybdates for Selective Oxidation of Propylene to Acrolein, in: Mater. Sci. Forum, Trans Tech Publ 804 (2015) 225–228.
- [13] R.K. Grasselli, Advances and future trends in selective oxidation and ammoxidation catalysis, Catal. Today 49 (1999) 141–153.
- [14] K. Schuh, W. Kleist, M. Høj, V. Trouillet, A.D. Jensen, J.–D. Grunwaldt, One-step synthesis of bismuth molybdate catalysts via flame spray pyrolysis for the selective oxidation of propylene to acrolein, Chem. Commun. 50 (2014) 15404–15406.
- [15] A.P.V. Soares, L.D. Dimitrov, M.–C.–R.–A. de Oliveira, L. Hilaire, M.F. Portela, R.K. Grasselli, Synergy effects between  $\beta$  and  $\gamma$  phases of bismuth molybdates in the selective catalytic oxidation of 1-butene, Appl. Catal., A 253 (2003) 191–200.
- [16] M.T. Le, V.H. Do, D.D. Truong, E. Bruneel, I. Van Driessche, A. Riisager, R. Fehrmann, Q.T. Trinh, Synergy Effects of the Mixture of Bismuth Molybdate Catalysts with SnO<sub>2</sub>/ZrO<sub>2</sub>/MgO in Selective Propene Oxidation and the Connection between Conductivity and Catalytic Activity, Ind. Eng. Chem. Res. 55 (17) (2016) 4846–4855.
- [17] J.F. Brazdil, Scheelite: a versatile structural template for selective alkene oxidation catalysts, Cat. Sci. Tec. 5 (7) (2015) 3452–3458.
- [18] Z. Zhai, M. Wütschert, R.B. Licht, A.T. Bell, Effects of catalyst crystal structure on the oxidation of propene to acrolein, Catal. Today 261 (2016) 146–153.
- [19] P. Sprenger, M. Stehle, A. Gaur, A.M. Gänzler, D. Gashnikova, W. Kleist, J.–D. Grunwaldt, Reactivity of Bismuth Molybdates for Selective Oxidation of Propylene Probed by Correlative Operando Spectroscopies, ACS Catal. 8 (7) (2018) 6462–6475.
- [20] M. Wolfs, P. Batist, The selective oxidation of 1-butene over a multicomponent molybdate catalyst. Influences of various elements on structure and activity, J. Catal. 32 (1974) 25–36.
- [21] I. Matsuura, M. Wolfs, X-ray photoelectron spectroscopy study of some bismuth molybdates and multicomponent molybdates, J. Catal. 37 (1975) 174–178.
- [22] W. Ueda, Y. Moro-Oka, T. Ikawa, I. Matsuura, Promotion effect of iron for the multicomponent bismuth molybdate catalysts as revealed by 18O<sub>2</sub> tracer, Chem. Lett. 11 (1982) 1365–1368.
- [23] O. Krylov, Y.V. Maksimov, L.Y. Margolis, In situ study of ferric molybdate rearrangement in partial propylene oxidation, J. Catal. 95 (1985) 289–292.
- [24] H. Ponceblanc, J.–M.–M. Millet, G. Coudurier, O. Legendre, J.C. Védrine, Solid-solid phase equilibria in the binary system cobalt molybdate (CoMoO<sub>4</sub>)-iron molybdate (FeMoO<sub>4</sub>) and effect of iron on the phase equilibria, J. Phys. Chem. 96 (1992) 9462–9465.
- [25] H. Ponceblanc, J.–M.–M. Millet, G. Coudurier, J.C. Védrine, Synergy effect of multicomponent Co, Fe, and Bi molybdates in propene partial oxidation, in: S.

- Oyama, J.W. Hightower (Eds.), *Catalytic Selective Oxidation*, ACS Publications, Washington, DC, pp. 262–272.
- [26] J.M.M. Millet, H. Ponceblanc, G. Coudurier, J.M. Herrmann, J.C. Vedrine, Study of multiphasic molybdate-based catalysts: II. Synergy effect between bismuth molybdates and mixed iron and cobalt molybdates in mild oxidation of propene, *J. Catal.* 142 (2) (1993) 381–391.
- [27] J. Engeldinger, J. Radnik, C. Kreyenschulte, F. Devred, E.M. Gaigneaux, A. Fischer, H.-W. Zanthoff, U. Bentrup, Probing the Structural Changes and Redox Behavior of Mixed Molybdate Catalysts under Ammoxidation Conditions: An Operando Raman Spectroscopy Study, *ChemCatChem* 8 (5) (2016) 976–983.
- [28] P. Sprenger, T. Sheppard, J.-P. Suuronen, A. Gaur, F. Benzi, J.-D. Grunwaldt, Structural Evolution of Highly Active Multicomponent Catalysts for Selective Propylene Oxidation, *Catalysts* 8 (2018) 356–376.
- [29] P. Sprenger, M. Stehle, A. Gaur, J. Weiß, D. Brueckner, Y.i. Zhang, J. Garrevoet, J.-P. Suuronen, M. Thomann, A. Fischer, J.-D. Grunwaldt, T.L. Sheppard, Chemical Imaging of Mixed Metal Oxide Catalysts for Propylene Oxidation: From Model Binary Systems to Complex Multicomponent Systems, *ChemCatChem* 13 (10) (2021) 2483–2493.
- [30] P. Mars, D.W. van Krevelen, Oxidations carried out by means of vanadium oxide catalysts, *Chem. Eng. Sci.* 3 (1954) 41–59.
- [31] G.W. Keulks, The mechanism of oxygen atom incorporation into the products of propylene oxidation over bismuth molybdate, *J. Catal.* 19 (1970) 232–235.
- [32] R. Wragg, P. Ashmore, J. Hockey, Selective oxidation of propene over bismuth molybdate catalysts: the oxidation of propene using 18O labeled oxygen and catalyst, *J. Catal.* 22 (1971) 49–53.
- [33] G.W. Keulks, L.D. Krenzke, T.M. Notermann, Selective oxidation of propylene, *Adv. Catal.* 27 (1979) 183–225.
- [34] Y. Moro-Oka, W. Ueda, K.-H. Lee, The role of bulk oxide ion in the catalytic oxidation reaction over metal oxide catalyst, *J. Mol. Catal. A: Chem.* 199 (2003) 139–148.
- [35] B. Benaichouba, P. Bussiere, J.C. Védrine, In-situ Mössbauer spectroscopic study of iron site evolution in iron and cobalt molybdates catalysts in propene oxidation reaction conditions, *Appl. Catal., A* 130 (1995) 31–45.
- [36] R.K. Grasselli, Genesis of site isolation and phase cooperation in selective oxidation catalysis, *Top. Catal.* 15 (2001) 93–101.
- [37] D.-H. He, W. Ueda, Y. Moro-Oka, Promotion effect of molybdate support on Bi<sub>2</sub>Mo<sub>3</sub>O<sub>12</sub> catalyst in the selective oxidation of propylene, *Catal. Lett.* 12 (1992) 35–44.
- [38] T.P. Rao, K. Krishnamurthy, Role of iron in multicomponent molybdate catalysts for selective oxidation of propylene, *J. Catal.* 95 (1985) 209–219.
- [39] O. Udalova, D. Shashkin, M. Shibanova, O. Krylov, Action of Co-Mo-Bi-Fe-Sb-K catalysts in the partial oxidation of propylene to acrolein: 1. The composition dependence of activity and selectivity, *Kinet. Catal.* 46 (2005) 535–544.
- [40] X. Wu, G. Yu, X. Chen, Y. Wang, C. Liu, Reduction/reoxidation of a multicomponent molybdate catalyst for propylene ammoxidation, *Thermochim. Acta* 486 (2009) 20–26.
- [41] L.-B. Wu, L.-H. Wu, W.-M. Yang, A.I. Frenkel, Study of the local structure and oxidation state of iron in complex oxide catalysts for propylene ammoxidation, *Cat. Sci. Tec.* 4 (8) (2014) 2512–2519.
- [42] H. Mehner, W. Meisel, Surface vs. bulk composition of an oxidic Fe-Mo multicomponent catalyst, *Mater. Sci. Eng., B* 25 (1) (1994) 1–4.
- [43] L. Mädler, H.K. Kammler, R. Mueller, S.E. Pratsinis, Controlled synthesis of nanostructured particles by flame spray pyrolysis, *J. Aerosol Sci.* 33 (2) (2002) 369–389.
- [44] J.-D. Grunwaldt, M. Caravati, S. Hannemann, A. Baiker, X-ray absorption spectroscopy under reaction conditions: suitability of different reaction cells for combined catalyst characterization and time-resolved studies, *Phys. Chem. Chem. Phys.* 6 (11) (2004) 3037, <https://doi.org/10.1039/b403071k>.
- [45] V. Briois, C. La Fontaine, S. Belin, L. Barthe, T.H. Moreno, V. Pinty, A. Carcy, R. Girardot, E. Fonda, ROCK: the new Quick-EXAFS beamline at SOLEIL, *J. Phys. Conf. Ser.* 712 (2016) 012149, <https://doi.org/10.1088/1742-6596/712/1/012149>.
- [46] C. La Fontaine, S. Belin, L. Barthe, O. Roudenko, V. Briois, ROCK: A Beamline Tailored for Catalysis and Energy-Related Materials from ms Time Resolution to  $\mu$ m Spatial Resolution, *Synchrotron Radiat. News* 33 (2020) 20–25.
- [47] B. Ravel, M. Newville, ATHENA, ARTEMIS, HEPHAESTUS: data analysis for X-ray absorption spectroscopy using IFFEFIT, *J. Synchrotron Radiat.* 12 (2005) 537–541.
- [48] V. Dyadkin, P. Pattison, V. Dmitriev, D. Chernyshov, A new multipurpose diffractometer PILATUS@ SNBL, *J. Synchrotron Radiat.* 23 (2016) 825–829.
- [49] A.A. Coelho, TOPAS and TOPAS-Academic: an optimization program integrating computer algebra and crystallographic objects written in C++, *J. Appl. Crystallogr.* 51 (2018) 210–218.
- [50] O. Glemser, R. Haeseler, Gasförmige hydroxide. IV. Über gasförmige hydroxide des molybdäns und wolframs, *Z. Anorg. Allg. Chem.* 316 (1962) 168–181.
- [51] L. Zhang, D. Liu, B. Yang, J. Zhao, Investigations of the mechanisms and kinetics leading to a loss of molybdenum from bismuth molybdate catalysts, *Appl. Catal., A* 117 (1994) 163–171.
- [52] D. Shashkin, O. Udalova, M. Shibanova, O. Krylov, The mechanism of action of a multicomponent Co-Mo-Bi-Fe-Sb-KO catalyst for the partial oxidation of propylene to acrolein: II. Changes in the phase composition of the catalyst under reaction conditions, *Kinet. Catal.* 46 (2005) 545–549.
- [53] G. Ganzer, H. Freund, Kinetic Modeling of the Partial Oxidation of Propylene to Acrolein: A Systematic Procedure for Parameter Estimation Based on Non-isothermal Data, *Ind. Eng. Chem. Res.* 58 (2019) 1857–1874.
- [54] A.M. Beale, S.D. Jacques, E. Sacaliuc-Parvalescu, M.G. O'Brien, P. Barnes, B.M. Weckhuysen, An iron molybdate catalyst for methanol to formaldehyde conversion prepared by a hydrothermal method and its characterization, *Appl. Catal., A* 363 (2009) 143–152.
- [55] J.A. Rodriguez, S. Chaturvedi, J.C. Hanson, A. Albornoz, J.L. Brito, Electronic properties and phase transformations in CoMoO<sub>4</sub> and NiMoO<sub>4</sub>: XANES and time-resolved synchrotron XRD studies, *J. Phys. Chem. B* 102 (1998) 1347–1355.
- [56] S.S. Saleem, Infrared and Raman spectroscopic studies of the polymorphic forms of nickel, cobalt and ferric molybdates, *Infrared Phys.* 27 (1987) 309–315.
- [57] E. Payen, M. Dhamelincourt, P. Dhamelincourt, J. Grimblot, J. Bonnelle, Study of Co (or Ni)-Mo oxide phase transformation and hydrodesulfurization catalysts by Raman microprobe equipped with new cells, *Appl. Spectrosc.* 36 (1982) 30–37.
- [58] R.K.S. Costa, S.C. Teles, K.P.F. Siqueira, The relationship between crystal structures and thermochromism in CoMoO<sub>4</sub>, *Chem. Papers* 75 (1) (2021) 237–248.
- [59] F.D. Hardcastle, I.E. Wachs, Molecular structure of molybdenum oxide in bismuth molybdates by Raman spectroscopy, *J. Phys. Chem.* 95 (1991) 10763–10772.
- [60] B. Mihailova, G. Bogachev, M. Gospodinov, L. Konstantinov, Raman spectroscopic study of Bi<sub>2</sub>(MoO<sub>4</sub>)<sub>3</sub>, *J. Raman Spectrosc.* 30 (1999) 195–198.
- [61] L. Seguin, M. Figlarz, R. Cavagnat, J.-C. Lassègues, Infrared and Raman spectra of MoO<sub>3</sub> molybdenum trioxides and MoO<sub>3</sub>·xH<sub>2</sub>O molybdenum trioxide hydrates, *Spectrochim. Acta A* 51 (1995) 1323–1344.
- [62] H. Tian, I.E. Wachs, L.E. Briand, Comparison of UV and visible Raman spectroscopy of bulk metal molybdate and metal vanadate catalysts, *J. Phys. Chem. B* 109 (2005) 23491–23499.
- [63] G. Jin, W. Weng, Z. Lin, N.F. Dummer, S.H. Taylor, C.J. Kiely, J.K. Bartley, G.J. Hutchings, Fe<sub>2</sub>(MoO<sub>4</sub>)<sub>3</sub>/MoO<sub>3</sub> nano-structured catalysts for the oxidation of methanol to formaldehyde, *J. Catal.* 296 (2012) 55–64.
- [64] A. Gaur, M. Stehle, K.V. Raun, J. Thrane, A.D. Jensen, J.-D. Grunwaldt, M. Høj, Structural dynamics of an iron molybdate catalyst under redox cycling conditions studied with in situ multi edge XAS and XRD, *Phys. Chem. Chem. Phys.* 22 (2020) 11713–11723.
- [65] W. Sears, W. Keeler, Optical measurements on heavily reduced bismuth iron molybdate: evidence for vacancy-induced phase transitions, *Appl. Spectrosc.* 46 (1992) 1898–1903.
- [66] P. Forzatti, P. Villa, N. Ferlazzo, D. Jones, Multicomponent catalysts for the oxidation of propylene to acrolein: Fe<sub>2</sub>(MoO<sub>4</sub>)<sub>3</sub> doped with Bi or Te, *J. Catal.* 76 (1982) 188–207.
- [67] A.W. Sleight, W. Jeitschko, Bi<sub>3</sub>(FeO<sub>4</sub>)(MoO<sub>4</sub>)<sub>2</sub> and Bi<sub>3</sub>(GaO<sub>4</sub>)(MoO<sub>4</sub>)<sub>2</sub> - new compounds with scheelite related structures, *Mater. Res. Bull.* 9 (7) (1974) 951–954.
- [68] Y. Moro-Oka, D.-H. He, W. Ueda, Catalyst oxide support oxide interaction to prepare multifunctional oxidation catalysts, in: R.K. Grasselli, A.W. Sleight (Eds.), *Stud. Elsevier, Surf. Sci. Catal.*, 1991, pp. 57–66.
- [69] J.F. Brazdil, D.D. Suresh, R.K. Grasselli, Redox kinetics of bismuth molybdate ammoxidation catalysts, *J. Catal.* 66 (1980) 347–367.
- [70] L.D. Krenzke, G.W. Keulks, The catalytic oxidation of propylene: VIII. An investigation of the kinetics over Bi<sub>2</sub>Mo<sub>3</sub>O<sub>12</sub>, Bi<sub>2</sub>MoO<sub>6</sub>, and Bi<sub>3</sub>FeMo<sub>2</sub>O<sub>12</sub>, *J. Catal.* 64 (1980) 295–302.
- [71] J. Brazdil, M. Mehicic, L. Glaeser, M. Hazle, R. Grasselli, Correlation between spectroscopic measurements and catalytic behavior of selective oxidation catalysts, in: M.L. Deviey, J.L. Gland (Eds.), *Catalyst Characterization Science*, ACS Publications, Washington, DC, 1985, pp. 26–36.
- [72] C. Lesage, E. Devers, C. Legens, G. Fernandes, O. Roudenko, V. Briois, High pressure cell for edge jumping X-ray absorption spectroscopy: Applications to industrial liquid sulfidation of hydrotreatment catalysts, *Catal. Today* 336 (2019) 63–73, <https://doi.org/10.1016/j.cattod.2019.01.081>.